








Thermal Equation of State and Structural Evolution of Al-Bearing Bridgmanite

Giacomo Criniti^{1,2} , Tiziana Boffa Ballaran¹, Alexander Kurnosov¹ , Zhaodong Liu³ , Konstantin Glazyrin⁴ , Marco Merlini⁵, Michael Hanfland⁶, and Daniel J. Frost¹ 

¹Bayerisches Geoinstitut, Universität Bayreuth, Universitätsstraße 30, Bayreuth, Germany, ²Now at Earth and Planets Laboratory, Carnegie Institution for Science, Washington, DC, USA, ³State Key Laboratory of Superhard Materials, Jilin University, Changchun, China, ⁴Deutsches Elektronen-Synchrotron DESY, Hamburg, Germany, ⁵Dipartimento di Scienze della Terra, Università degli Studi di Milano, Via Botticelli 23, Milano, Italy, ⁶ESRF – European Synchrotron Radiation Facility, Grenoble, France

Key Points:

- The thermal equation of state of Al-bearing bridgmanite was determined for the first time using single crystals
- The bulk compressibility of Al-bearing bridgmanite is mostly controlled by Al-Si substitution in the octahedral site
- Using the obtained equation of state parameters, we modeled the pressure dependency of oxygen vacancies in bridgmanite in MgO–AlO_{1.5}–SiO₂

Supporting Information:

Supporting Information may be found in the online version of this article.

Correspondence to:

G. Criniti,
giacomo.criniti@uni-bayreuth.de

Citation:

Criniti, G., Boffa Ballaran, T., Kurnosov, A., Liu, Z., Glazyrin, K., Merlini, M., et al. (2024). Thermal equation of state and structural evolution of Al-bearing bridgmanite. *Journal of Geophysical Research: Solid Earth*, 129, e2023JB026879. <https://doi.org/10.1029/2023JB026879>

Received 12 APR 2023

Accepted 19 DEC 2023

Author Contributions:

Conceptualization: Giacomo Criniti, Tiziana Boffa Ballaran
Data curation: Giacomo Criniti
Formal analysis: Giacomo Criniti, Tiziana Boffa Ballaran
Funding acquisition: Daniel J. Frost
Investigation: Giacomo Criniti, Tiziana Boffa Ballaran, Alexander Kurnosov, Zhaodong Liu, Konstantin Glazyrin, Marco Merlini, Michael Hanfland
Methodology: Giacomo Criniti, Tiziana Boffa Ballaran, Alexander Kurnosov, Zhaodong Liu, Konstantin Glazyrin, Marco Merlini, Michael Hanfland

Abstract (Mg, Fe, Al)(Si, Al)O₃ bridgmanite is the most abundant mineral of Earth's lower mantle. Al is incorporated in the crystal structure of bridgmanite through the Fe³⁺AlO₃ and AlAlO₃ charge coupled (CC) mechanisms, and the MgAlO_{2.5} oxygen vacancy (OV) mechanism. Oxygen vacancies are believed to cause a substantial decrease of the bulk modulus of aluminous bridgmanite based on first-principles calculations on the MgAlO_{2.5} end-member. However, there is no conclusive experimental evidence supporting this hypothesis due to the uncertainties on the chemical composition, crystal chemistry, and/or high-pressure behavior of samples analyzed in previous studies. Here, we synthesized high-quality single crystals of bridgmanite in the MgO–AlO_{1.5}–SiO₂ system with different bulk Al contents and degrees of CC and OV substitutions. Suitable crystals with different compositions were loaded in resistively heated diamond anvil cells and analyzed by synchrotron X-ray diffraction at pressures up to approximately 80 GPa at room temperature and 35 GPa at temperatures up to 1,000 K. Single-crystal structural refinements at high pressure show that the compressibility of bridgmanite is mainly controlled by Al–Si substitution in the octahedral site and that oxygen vacancies in bridgmanite have no detectable effect on the bulk modulus in the compositional range investigated here, which is that relevant to a pyrolytic lower mantle. The proportion of oxygen vacancies in Al-bearing bridgmanite has been calculated using a thermodynamic model constrained using experimental data at 27 GPa and 2,000 K for an Fe-free system and extrapolated to pressures equivalent to 1,250 km depth using the thermoelastic parameters of Al-bearing bridgmanite determined in this study.

Plain Language Summary Earth's lower mantle, spanning from approximately 660 to 2,890 km depth, is mainly composed of bridgmanite, (Mg, Fe, Al)(Si, Al)O₃ with a distorted perovskite-type structure. In the topmost 500 km of the lower mantle, experiments showed that an MgAlO_{2.5} oxygen vacancy component may be present in bridgmanite. However, the effect of oxygen vacancies on the thermoelastic properties of bridgmanite is still not well constrained. These parameters are of crucial importance not only to model the thermodynamic stability of bridgmanite components at high-pressure and high-temperature but also to calculate the physical properties of lower mantle rocks. Here, we have determined the high-pressure and high-pressure-temperature equations of state of three bridgmanite samples having different concentrations of Al and oxygen vacancies using X-ray diffraction in diamond anvil cells. These data are complemented by the analysis of the bridgmanite crystal structure as a function of pressure, which revealed that oxygen vacancies have a minor effect on the elastic properties of bridgmanite at concentrations relevant for the lower mantle. Combining our results with experimental data on the stability of bridgmanite in the MgO–AlO_{1.5}–SiO₂ system, we have modeled the thermodynamic stability of the MgAlO_{2.5} component as a function of pressure and bulk Al content.

1. Introduction

Bridgmanite, MgSiO₃ with a distorted perovskite structure, is the most abundant mineral phase in Earth's interior and constitutes approximately 80 vol.% of the lower mantle (Irifune et al., 2010; Kurnosov et al., 2017). The structure of bridgmanite comprises a framework of corner-sharing SiO₆ octahedra (B site), which form large 12-fold coordinated cavities that are filled by Mg (A site). High-pressure experiments indicate that Al and Fe account for the main chemical substitutions in bridgmanite at lower mantle conditions and their incorporation mechanism

© 2024. The Authors.

This is an open access article under the terms of the [Creative Commons Attribution License](https://creativecommons.org/licenses/by/4.0/), which permits use, distribution and reproduction in any medium, provided the original work is properly cited.

Supervision: Tiziana Boffa Ballaran, Daniel J. Frost

Writing – original draft: Giacomo Criniti

Writing – review & editing: Tiziana Boffa Ballaran, Alexander Kurnosov, Zhaodong Liu, Konstantin Glazyrin, Marco Merlini, Michael Hanfland, Daniel J. Frost

depends on pressure, temperature, oxygen fugacity, and the bulk chemical composition of the system (Huang, Boffa Ballaran, McCammon, Miyajima, Dolejš, et al., 2021). Al can substitute for both Si and Mg in the B and A sites, respectively, through the charge coupled (CC) substitution of the components AlAlO_3 and $\text{Fe}^{3+}\text{AlO}_3$, and the oxygen vacancy (OV) substitution of $\text{MgAlO}_{2.5}$ (Navrotsky et al., 2003; Vanpeteghem et al., 2006). The concentration of the OV component in bridgmanite was found to reach a maximum at topmost lower mantle conditions in MgO saturated systems, and to rapidly decay with increasing pressure and Al_2O_3 content (Z. Liu, Boffa Ballaran, et al., 2019; Z. Liu, Ishii, et al., 2017). The near absence of oxygen vacancies at pressures above 40 GPa was argued to affect not only the elastic properties but also the transport properties of bridgmanite (Z. Liu, Ishii, et al., 2017), which may account for a possible increase in viscosity of the mid-mantle, proposed to occur at approximately 1,000 km depth (Rudolph et al., 2015). It follows that the ability to model the crystal chemistry of bridgmanite as a function of pressure, temperature and composition is of pivotal importance for understanding mantle dynamics and building internally consistent thermodynamic and mineral physical models for comparison with geophysical observations (Criniti et al., 2021; Kurnosov et al., 2017). To date, however, the resolution of such models of the lower mantle is limited by the lack of experimental data on the thermoelastic parameters of bridgmanite and by uncertainties on thermodynamic parameters that describe its pressure- and temperature-dependent element partitioning with other phases. For instance, the effect of CC and OV Al-substitutions on the thermoelastic parameters of bridgmanite is still controversial. A previous computational study suggested the OV component to be much softer than MgSiO_3 (Brodholt, 2000). This could explain some observations on the compressibility of Al-bearing bridgmanite made using powder X-ray diffraction measurements in the diamond anvil cell (DAC) (Daniel et al., 2001; Yagi et al., 2004; Zhang & Weidner, 1999). Other DAC studies, on the other hand, have found that Al has a much milder effect on the compressibility of bridgmanite, which was found to be either slightly higher or slightly lower than that of the MgSiO_3 end-member (Andraut et al., 2001, 2007; Daniel et al., 2004; Jackson et al., 2005; Walter et al., 2004, 2006). The contrasting results presented in previous studies may arise in part from the poor chemical characterization of the samples, which were often synthesized and compressed in the same DAC run (Andraut et al., 2001, 2007; Walter et al., 2004, 2006) and partly from the limited and sometimes discontinuous pressure range investigated (Andraut et al., 2001, 2007; Walter et al., 2004; Yagi et al., 2004), which in some instances did not even reach pressures of the bridgmanite stability field (Walter et al., 2006; Zhang & Weidner, 1999). As a result, the thermoelastic parameters of Al-bearing bridgmanite remain largely unconstrained, hampering our ability to model the stability of the CC and OV components in the lower mantle, as well as their effect on the seismic properties of the bridgmanite solid solution.

Single-crystal X-ray diffraction is a powerful tool for determining the thermal equation of state of materials in the DAC. This technique allows not only high-quality unit-cell lattice parameters of materials at high pressure and temperature to be obtained, but also enables unique information on their crystal structures to be retrieved with higher accuracy and precision than powder diffraction measurements. This opens the possibility of determining the individual effects of different Al-substitutions through a detailed examination of the relationship between crystal chemistry, structural evolution, and compressibility of bridgmanite. Here, we report the thermal equation of state of Fe-free Al-bearing bridgmanite, determined by single-crystal X-ray diffraction at high pressure and high temperature using externally heated DACs. Each of the studied samples was synthesized in a multi-anvil apparatus and its composition was determined using high quality analyses employing secondary standards prior to the compression experiments. From the refinement of more than 100 crystal structures of Al-bearing bridgmanite and MgSiO_3 bridgmanite (original data set collected by Boffa Ballaran et al., 2012) at high-pressure conditions, we then derived the relation between Al-substitution, polyhedral compressibility, and bulk compressibility. Equation of state parameters obtained in this study are compared primarily with those determined in previous single-crystal studies, using well characterized samples synthesized in a multi-anvil press, and studies employing polycrystalline samples whose chemical composition was determined before or after the compression study. The determined solid solution behavior between MgSiO_3 , AlAlO_3 , and $\text{MgAlO}_{2.5}$ bridgmanite components was finally used to model the stability of oxygen vacancies in the $\text{MgO}-\text{AlO}_{1.5}-\text{SiO}_2$ system as a function of pressure, temperature, and composition.

2. Experimental Methods

2.1. Sample Synthesis and Characterization

Single crystals of Fe-free Al-bearing bridgmanite were synthesized at 24 GPa and 1,773–1,973 K (Table 1) using a 1,200-tonne split-sphere-type multi-anvil apparatus installed at the Bayerisches Geoinstitut, University of Bayreuth

Table 1
Synthesis Conditions and Chemical Compositions of Al-Bearing Bridgmanite Samples

Run	Starting material	Flux	P (GPa)	T (K)	t (hr)	Run products	Oxide composition (wt.%)			
							MgO	SiO ₂	AlO _{1.5}	Total
I701	En95-Cor5	Mg(OH) ₂	28	1,973	6	Brg + Hym	38.50(26)	58.06(68)	4.96(42)	99.53(62)
S7412	En90-Cor10	MgCl ₂	24	1,873	4	Brg + Clm ± Grt	37.60(64)	53.26(73)	9.28(59)	100.1(11)
S7464	En95-Cor5	MgCl ₂	24	1,973	3	Brg + Clm	39.35(50)	55.48(52)	5.21(47)	100.08(62)
S7585	En85-Cor15	MgCl ₂	24	1,773	8	Brg + Clm ± Grt	37.45(34)	53.78(50)	8.54(32)	99.83(49)
		Atoms per 2 cations			End-member composition					
	Mg	Al	Si	O	CC	OV	Label			
I701	0.962(6)	0.098(8)	0.940(7)	2.989(6)	0.038(6)	0.022(11)	CC4OV2			
S7412	0.932(9)	0.182(11)	0.886(9)	2.977(7)	0.068(9)	0.046(14)	CC7OV5			
S7464	0.975(10)	0.102(9)	0.922(6)	2.974(7)	0.025(7)	0.053(11)	CC2OV5			
S7585	0.932(6)	0.168(7)	0.899(6)	2.983(6)	0.067(6)	0.034(9)	CC7OV3			

Note. En, enstatite; Cor, corundum; Brg, bridgmanite; Hym, hydrous melt; Clm, Cl-rich melt; Grt, garnet (traces).

(Keppler & Frost, 2005). The starting material consisted of finely ground mixtures of synthetic MgSiO₃ enstatite and reagent grade Al₂O₃ corundum in different molar ratios (Table 1). To synthesize the MgSiO₃ enstatite powder, a glass with the same composition was obtained by heating a stoichiometric mixture of reagent grade SiO₂ and MgO at 1,873 K in a furnace for 6 hr. The MgSiO₃ glass was then ground for 1 hr in an agate mortar under ethanol and then heated in a furnace at 1,473 K for 5 hr. To confirm that the glass had converted to enstatite, a powder X-ray diffraction pattern of the recovered material was collected on a Philips X'Pert Pro diffractometer equipped with Co-Kα1 radiation operated at 40 kV and 40 mA monochromatized with a curved Johansson Ge₍₁₁₁₎ crystal and a Philips X'celerator detector. The MgSiO₃-Al₂O₃ mixtures were loaded in 2 mm long Pt-tube capsules together with approximately 10–20 vol.% of reagent grade MgCl₂ that served as flux material to facilitate crystal growth at high pressure and temperature conditions. As MgCl₂ is highly hygroscopic, it was stored in an oven at 423 K for at least 12 hr before being used and was loaded in the Pt-capsule while still warm. Each capsule was then immediately closed with Pt-lids and sealed using an arc welder to prevent MgCl₂ from adsorbing water from air moisture. To generate high-pressure and high-temperature conditions, tungsten carbide (WC, 7 wt.% Co content) cubes with 3 mm corner truncations were used with a 7 mm edge-length octahedral Cr₂O₃-doped MgO pressure medium (7/3 assembly) that contained a cylindrical LaCrO₃ heater. The capsule was then enclosed in an MgO sleeve to avoid contact with the LaCrO₃ heater and placed at the center of the octahedral pressure medium. The cell assembly was first compressed to the desired press load and then heated at a rate of 100 K per minute until the target temperature was reached. The temperature was estimated based on the power supplied to the LaCrO₃ heater, which had been calibrated in previous runs. Experimental conditions are reported in Table 1. After heating, the experiment was quenched by cutting the electrical power and slowly decompressed to ambient conditions over 15 hr. One additional experimental run (I701) was performed at 28 GPa in the 15-MN Kawai-type multi-anvil press IRIS15 (Ishii et al., 2016, 2019; Z. Liu, Nishi, et al., 2017) installed at the Bayerisches Geoinstitut, University of Bayreuth. In this run, harder WC anvils were used (grade TF05, Fuji Die Co. Ltd) with the same type of 7/3 assembly. The starting material for this experiment consisted of a mixture of MgSiO₃ enstatite, Al₂O₃ corundum and Mg(OH)₂ brucite (Table 1). The temperature was also estimated based on the power supplied to the LaCrO₃ heater, which was calibrated in previous runs.

The recovered samples were observed under an optical microscope and consisted of mixtures of Al-bearing bridgmanite crystals up to 100 μm in size and quenched Cl-rich (S7412, S7464, S7585) or hydrous melt (I701). In experimental runs at 24 GPa with a relatively Al₂O₃-rich starting composition (i.e., S7412, S7585), minor amounts of garnet were also found in the run products. Inclusion-free single crystals of Al-bearing bridgmanite larger than 60 μm were selected from each crystal batch and mounted on glass fibers for single-crystal X-ray diffraction analyses at ambient conditions. Several crystals were tested on a kappa-geometry Xcalibur single-crystal diffractometer equipped with a Sapphire2 charge-coupled device (CCD) detector and graphite-monochromatized Mo-Kα1 radiation operated at 50 kV and 40 mA. For each batch, the single crystal displaying the sharpest peak profiles was then analyzed on a Eulerian-geometry Huber diffractometer equipped with a point detector and using Mo-Kα radiation operated at 50 kV and 40 mA, and driven by the software SINGLE (Angel & Finger, 2011). The peaks

full width half maxima measured upon ω -scan rotations typically ranged between 0.07° and 0.11° . The unit-cell lattice parameters, reported in Table S1 in Supporting Information S1, were accurately and precisely determined by a least square inversion of 16–32 reflections measured at eight equivalent positions (King & Finger, 1979; Ralph & Finger, 1982). The chemical compositions of several selected single crystals (Table 1) were measured using a JEOL JXA-8200 electron probe microanalyzer (EPMA) operated in wavelength dispersive mode. Spectra were acquired for 10 s using an acceleration voltage and beam current of 15 kV and 5 nA, respectively. MgSiO_3 enstatite was used as a standard for Si and Mg, Al_2O_3 corundum for Al, and $\text{Pb}_5(\text{VO}_4)_3\text{Cl}$ vanadinite for Cl. Accurately determining the Mg/Si ratio of the bridgmanite samples is critical to evaluate the concentration of oxygen vacancies. Following the procedure proposed by Huang, Boffa Ballaran, McCammon, Miyajima, Dolejš, et al. (2021), a single crystal of MgSiO_3 akimotoite was used as a secondary standard and the EPMA was recalibrated until a Mg/Si ratio of 1.00 was obtained for this standard. The Cl contents of the samples synthesized using a MgCl_2 flux were below the detection level (<0.001 atoms per formula unit) and are thus not reported in Table 1. The water content of the sample recovered from 28 GPa was not directly measured but was assumed to be negligible (i.e., less than 50 ppm wt.) based on Fourier transform infrared spectroscopy measurements of bridgmanite single crystals previously synthesized using the same conditions and strategy (Z. Liu et al., 2021). Despite differences in temperature, pressure, and duration of the peak P - T conditions (Table 1), all samples proved to be chemically homogenous and free of chemical zoning. The composition of Al-bearing bridgmanite samples in terms of their end-member components MgSiO_3 , AlAlO_3 (CC) and $\text{MgAlO}_{2.5}$ (OV) were determined from their chemical formulas normalized to two cations, according to the relations proposed by Z. Liu, Boffa Ballaran, et al. (2019): $\text{Mg}_x\text{Al}_z\text{Si}_y\text{O}_{x+1.5z+2y}$ with $y = \text{MgSiO}_3$, $x - y = \text{MgAlO}_{2.5}$, and $(z - x + y)/2 = \text{AlAlO}_3$ (Table 1). Samples synthesized in runs I701 and S7464 exhibited the same bulk Al content within uncertainty but different concentrations of CC and OV components. The significantly lower OV component in the 28 GPa sample (I701) can most likely be attributed to the use of a hydrous flux rather than the higher pressure, which should have been insufficient to cause this reduction (Z. Liu, Ishii, et al., 2017). The hydrous flux likely renders a higher silica-activity than the samples produced using MgCl_2 . All MgCl_2 fluxed samples were relatively enriched in the OV component even at high bulk Al contents, which have been previously considered to favor the CC substitution mechanism (Z. Liu, Boffa Ballaran, et al., 2019; Z. Liu, Nishi, et al., 2017), and their OV contents may simply increase with increasing temperature (Z. Liu, Akaogi, et al., 2019).

2.2. High-Pressure and High-Temperature X-Ray Diffraction Measurements

Al-bearing bridgmanite samples with compositions CC4OV2, CC2OV5 and CC7OV3 (see Table 1) were employed in high-pressure DAC experiments aimed at constraining their isothermal and/or thermal equation of state. Single-crystal X-ray diffraction measurements at high pressure and temperature were carried out during several runs (Table 2) at the Extreme Conditions Beamline (ECB) P02.2 of the PETRA-III synchrotron facility (Hamburg, Germany) using an X-ray beam of 42.7 keV ($\lambda \sim 0.29 \text{ \AA}$) focused to either 2×2 or $8 \times 3 \text{ \mu m}^2$ (full width at half maximum) and a Perkin Elmer XRD 1621 flat panel detector (Liermann et al., 2015). The sample to detector distance and detector parameters for single-crystal diffraction were calibrated using polycrystalline CeO_2 and a single crystal of natural enstatite, respectively. To generate high-pressure conditions, we employed BX-90 DACs (Kantor et al., 2012) in combination with Almax-Boehler-type diamond anvils and WC seats (Boehler

Table 2

Conditions of the High-Pressure Room-Temperature and High-Pressure, High-Temperature (HT) Runs

Run	Sample(s)	Pressure medium	Culet size (μm)	P sensor(s)	P Range (GPa)	T Range (K)	P - T determination
RT1	CC2OV5, CC4OV2	He	350	ruby, Au	0–22	300	–
RT2	CC2OV5, CC4OV2	He	350	ruby, Au	0–50	300	–
RT3	CC7OV3	He	250	ruby, W	0–80	300	–
HT1	CC2OV5, CC4OV2	Ne	350	ruby, Au, W	0–26	300–500	Au + W + ruby ^a
HT2	CC2OV5, CC4OV2	Ne	400	ruby, Au, W	0–29	300–700	Au + TC
HT4	CC2OV5, CC4OV2	Ne	400	ruby, Au	0–21	300–460	Au + ruby ^a
HT5	CC2OV5, CC4OV2	Ne	350	ruby, Au, W	0–35	300–1,000	Au + TC

Note. TC, thermocouple; P , pressure; T , temperature.

^aDue to an inaccurate TC readout, a cross correlation of ruby and Au sensors or ruby, Au, and W sensors was used to determine P and T .

& De Hantsetters, 2004), which allowed effective X-ray opening angles of approximately 75–80°. Al-bearing bridgmanite single crystals with lengths of 10–20 μm and less than 10 μm thick were tested at ambient conditions at the ECB P02.2 and selected based on their sharp diffraction peak profiles. Suitable crystals were then loaded in the DACs for high-pressure measurements. For Room-Temperature (RT) runs (RT1–RT3), a Re gasket was indented between diamond anvils with culets of 350 or 250 μm (Table 2) to a final thickness of approximately 60 or 45 μm , respectively. To create the sample chamber, an infrared laser was used to drill a hole of 200 or 150 μm diameter, respectively, in the center of the indented area of the Re gasket. One (CC7OV3, run RT3) or two (CC2OV4 and CC2OV5, run RT1 and RT2) bridgmanite crystals were loaded into the sample chamber together with a ruby sphere for pressure determination and a piece of Au or W, whose absorption profiles were used to finely align the cell using the X-ray beam (Table 2). He or Ne gas (Table 2) were loaded into the sample chamber at 0.13 GPa using the gas loading system installed at the Bayerisches Geoinstitut, University of Bayreuth (Kurnosov et al., 2008) or at PETRA-III. The samples were compressed on line at RT using a gas-driven membrane up to 50 (CC2OV4, CC2OV5) or 80 GPa (CC7OV3) with typical steps of 1–3 GPa. At each pressure point, step scans were collected upon continuous ω -rotation of the DAC between $\pm 35^\circ$ with steps of 0.5° and an exposure time of 0.5–1 s.

Several high-pressure and high-temperature runs (Table 2) were carried out in DACs equipped with external resistive heaters (Y. Fei & Mao, 1994) by using 0.4–0.5 mm thick Pt-wire, instead of Mo, wrapped around a MACOR® (Corning Inc.) ceramic ring (de Grouchy et al., 2017; Pamato et al., 2016). Almax-Boehler diamond anvils with 350 or 400 μm culets were employed to generate high-pressure conditions. The ceramic ring and Pt-wire heater were placed around the WC seat in the BX-90 piston and fixed using cement. In order to prevent the heater from touching the BX-90 cylinder, a thin layer of mica was placed on top of the ceramic ring and acted as an electrical insulator. The Pt-wire was then connected to a Type 6674A DC power supply from Agilent Technology, capable of generating up to 35 A at 60 V (Liermann et al., 2015). Temperature was monitored using a Pt/Pt-10%Rh (Type S) thermocouple that was passed through a hole drilled in the ceramic ring and placed as close as possible to the sample chamber. A Re gasket was indented to 45–50 μm thickness and a 150 μm hole was laser-drilled in the center of the indented region to obtain the sample chamber. Two selected Al-bearing bridgmanite crystals with compositions CC2OV4 and CC2OV5 were loaded in each sample chamber together with a ruby sphere, Au powder and a piece of W that were used as pressure standards (Table 2). Pre-compressed Ne gas at 0.12 GPa was loaded in the sample chamber using the gas loading system installed at PETRA-III. Resistively heated DACs (RHDACs) were inserted into a membrane cup and pressure was increased on line using a gas-driven membrane. In addition, to prevent the oxidation of the heater components, diamond anvils and Re gasket, an Ar-H₂ gas mixture was flushed inside the RHDAC through an aperture drilled on one side of the membrane cup. The RHDAC was then placed in a custom-designed holder consisting of a water-cooled lower metallic body, a central ceramic insulator and a top metallic body where the membrane cup was fixed (Figure S1 in Supporting Information S1). In this way, the efficiency of the heater is enhanced, and higher temperatures can be generated. At each pressure-temperature point, step scans were collected upon continuous ω -rotation of the DAC between $\pm 32^\circ$, following the same procedure described above for RT measurements. Additional wide-scan images of mosaic W single crystals between $\omega = \pm 20^\circ$ or still frames of polycrystalline Au were acquired. 2D images were integrated into 1D patterns using the software *DIOPTAS* (Prescher & Prakapenka, 2015) and the lattice parameters of Au and W were obtained from full-profile Le Bail refinements performed in *JANA2006* (Petříček et al., 2014).

For runs HT2 and HT4, the unit-cell parameters of gold together with the temperature reading from the thermocouple were used to determine pressure at high temperature employing the thermal equation of state of Au reported by Dorogokupets and Dewaele (2007). In runs HT1 and HT4, the temperature readout of the thermocouple was found to be several hundred K higher than what we expected from the power generated by the Pt-wire heater. In these runs therefore a cross-correlation function between ruby and Au or ruby, Au and W (Table 2) was used to determine both pressure and temperature (see Text S1 and Figure S2 in Supporting Information S1). To account for potential systematic deviations that may be caused by using a cross-correlation function instead of the thermocouple, the temperature and pressure uncertainties in the two mentioned runs were rescaled to have smaller weights in the equations of state (EOS) fitting procedure.

2.3. Single-Crystal Structural Refinements

Single-crystal X-ray diffraction step-scans were analyzed using *CrysAlisPro* (Rigaku, Oxford Diffraction) to extract Al-bearing bridgmanite unit-cell lattice parameters at high-pressure conditions. Data analysis included peak search and indexing, background subtraction, integration of intensities and correction for Lorentz and polar-

ization factors. Frame scaling and empirical absorption correction based on spherical harmonics were carried out using the *SCALE3 ABSPACK* scaling algorithm implemented in *CrysAlisPro*. We then employed the dual space algorithm *SHELXT* (Sheldrick, 2015b) to solve the structures of Al-bearing bridgmanite crystals and performed structural refinements against F^2 using *SHELXL* in the *Shelxle* graphic user interface (GUI) (Hübschle et al., 2011; Sheldrick, 2015a). In the refinement procedure, atomic scattering factors were used for all atoms, while the site occupancy factors for Mg, Al and Si cations in the A and B sites were fixed according to the abundancies of the bridgmanite end-member components determined by EPMA (Table 1). Given that the number of unique reflections typically exceeded 250, anisotropic displacement parameters (ADPs) were used for all atoms, resulting in a total of 29 refined parameters. When the ratio of unique reflections to refined parameters dropped below six or one of the ADPs showed negative values, isotropic displacement parameters were used instead. In the last cycle of each refinement, the crystallographic $R1$ factors were typically between 2% and 3% and rarely exceeded 4%, highlighting the high quality of the data sets and the robustness of the structural models. In addition, structural refinements at high pressure and RT for MgSiO₃ bridgmanite were obtained using the data sets reported and described by Boffa Ballaran et al. (2012), by applying the same refinement procedure described above. Given the longer wavelength ($\lambda = 0.4147 \text{ \AA}$) employed by Boffa Ballaran et al. (2012), the number of observed and unique reflections for MgSiO₃ bridgmanite was smaller than for measurements performed in this study ($\lambda = 0.2900, 0.2905, \text{ or } 0.2908 \text{ \AA}$). Therefore, isotropic displacement parameters were used for all atoms in the structural refinements of MgSiO₃ bridgmanite. Further details can be found in the deposited crystallographic information files.

3. Isothermal Equation of State of Al-Bearing Bridgmanite

3.1. Volume and Axial Compressibility

The unit-cell volume and lattice parameters of Al-bearing bridgmanite samples (Tables S2–S4) were found to decrease smoothly with increasing pressure (Figure 1). We used third-order Birch-Murnaghan (BM3) EOS to fit the pressure-volume data sets (Angel et al., 2014; Birch, 1947):

$$P = \frac{3}{2} K_{T0} \left[\left(\frac{V_0}{V} \right)^{\frac{7}{3}} - \left(\frac{V_0}{V} \right)^{\frac{5}{3}} \right] \left\{ 1 + \frac{3}{4} (K'_{T0} - 4) \left[\left(\frac{V_0}{V} \right)^{\frac{2}{3}} - 1 \right] \right\} \quad (1)$$

Where V_0 , K_{T0} , and K'_{T0} are the room-pressure and RT unit-cell volume, the isothermal bulk modulus, and its pressure derivative. Fits were performed using a script implemented in OriginPro 2021 (OriginLab corporation, Northampton, MA, USA) that was previously benchmarked with the EosFit7-GUI software (Angel et al., 2014;

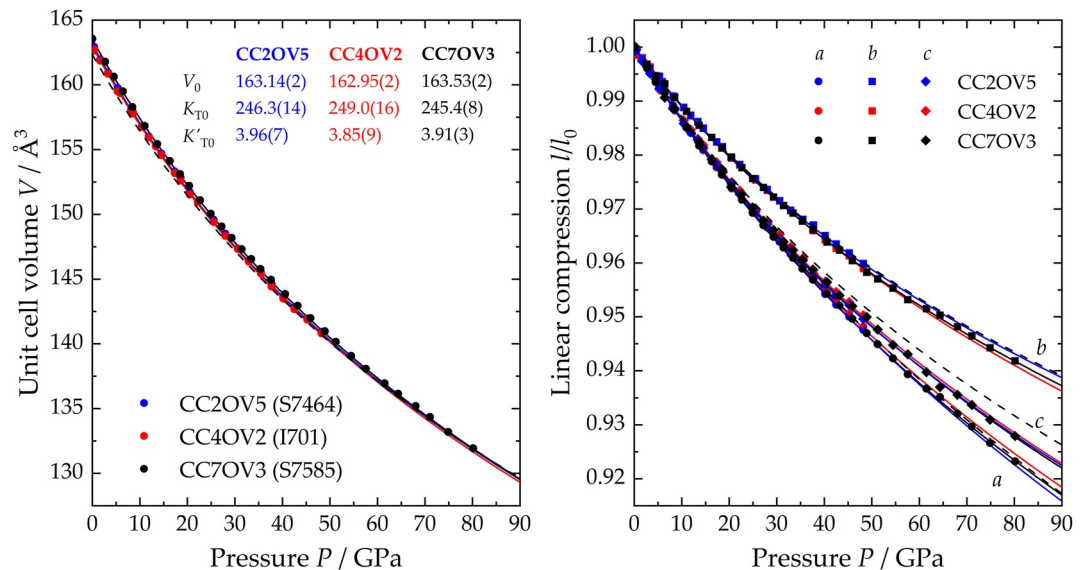


Figure 1. (a) Volume and (b) linear compression of Al-bearing bridgmanite samples at RT. Error bars are smaller than the symbol when they are not shown. Solid lines indicate BM3 fits to the experimental pressure-volume data sets of CC2OV5 (blue), CC4OV2 (red) and CC7OV3 (black). Dashed black lines indicate BM3 fits to the pressure-volume data set of MgSiO₃ bridgmanite reported by Boffa Ballaran et al. (2012).

Table 3
Isothermal Equations of State Parameters for Single-Crystal Al-Bearing Bridgmanite and MgSiO₃ Bridgmanite From Boffa Ballaran et al. (2012)

	CC2OV5	CC4OV2	CC7OV3	MgSiO ₃ ^a
BM3				
V_0 (Å ³)	163.14(2)	162.95(2)	163.53(2)	162.36(4)
K_{T0} (GPa)	246.3(14)	249.0(16)	245.4(8)	251(2)
K'_{T0}	3.96(7)	3.85(9)	3.91(3)	4.11(7)
a_0 (Å)	4.7762(4)	4.7798(3)	4.7737(3)	4.7757(3)
M'_{a0} (GPa)	708(7)	693(5)	688(4)	715(4)
M'_{a0}	8.9(3)	10.1(3)	9.81(13)	9.2(2)
b_0 (Å)	4.9362(3)	4.9333(3)	4.9388(4)	4.9285(5)
M'_{b0} (GPa)	840(9)	865(10)	836(8)	848(13)
M'_{b0}	16.6(5)	13.7(6)	15.6(3)	16.7(7)
c_0 (Å)	6.9199(6)	6.9106(3)	6.9364(12)	6.8970(3)
M'_{c0} (GPa)	685(7)	703(5)	690(9)	721(4)
M'_{c0}	12.0(4)	11.6(3)	11.7(3)	12.7(2)
BM2				
V_0 (Å ³)	163.14(2)	162.97(2)	163.57(2)	162.31(3)
K_{T0} (GPa)	245.6(3)	246.3(4)	243.2(3)	254.5(6)

^aAxial compressibility parameters of MgSiO₃ bridgmanite were obtained by refitting the data reported by Boffa Ballaran et al. (2012).

Gonzalez-Platas et al., 2016). Fit results are reported in Table 3. Despite showing small differences in K_{T0} and K'_{T0} , the EOSs of the three samples are relatively similar to each other, owing to the negative correlation coefficient between these two fit parameters (Figure S3 in Supporting Information S1). Since the refined K'_{T0} values for the three Al-bearing bridgmanite samples are close to 4, a 2nd-order Birch-Murnaghan EOS was also used to fit the three data sets (Table 3). The BM2 K_{T0} values of the CC2OV5 and CC7OV3 samples are identical to their respective BM3 values within the uncertainties, while for the CC4OV2 sample the BM2 K_{T0} value is approximately 3 GPa lower than its BM3 counterpart due to the fact that this sample has a smaller BM3 K'_{T0} (Table 3). As discussed later, these subtle variations in K_{T0} seem to be correlated with the Al-Si substitution at the B site, which influences its compressibility.

The axial compression of the three Al-bearing bridgmanite samples was described using a linearized BM3 EOS (Angel, 2000; Angel et al., 2014), which was originally derived for cubic and isotropic materials by considering that $V = a^3$ and $\beta_V = 3\beta_a$, with β_V and β_a being the volume and a -axis compressibility, respectively. This notation can be generalized for lower-symmetry materials by replacing the fit parameters V_0 , K_{T0} and K'_{T0} with the cubed unit cell edge length l_0^3 , the axial modulus $M_0/3$ and its pressure derivative $M'_0/3$ (Angel et al., 2014):

$$P = \frac{1}{2} M_{l,0} \left[\left(\frac{l_0}{l} \right)^7 - \left(\frac{l_0}{l} \right)^5 \right] \left\{ 1 + \frac{1}{4} (M'_{l,0} - 12) \left[\left(\frac{l_0}{l} \right)^2 - 1 \right] \right\} \quad (2)$$

Fit parameters for the three Al-bearing samples measured in this study, as well as for MgSiO₃ bridgmanite by Boffa Ballaran et al. (2012), are reported in Table 3. It can be seen that the b -axis is the most incompressible direction, while the a -axis is slightly more compressible than the c -axis for all samples. As the axial compressibility is particularly sensitive to non-hydrostatic stresses, we limit our comparison with previous work only to single crystals synthesized in a multi-anvil press and compressed in a DAC under quasi-hydrostatic conditions. The axial compressibility scheme determined in this study is in agreement with previous static compression (Boffa Ballaran et al., 2012) and elasticity measurements (Criniti et al., 2021; Sinogeikin et al., 2004) of single-crystal MgSiO₃ bridgmanite. For the Al-bearing experiments, the compressibility of the c -axis is higher than in MgSiO₃, as also observed for the Fe³⁺AlO₃ substitution mechanism (Boffa Ballaran et al., 2012), confirming that the Al-Si substitution at the B site plays a critical role in determining the stiffness of this direction.

3.2. Polyhedral and Bond Length Compressibility

By refining the crystal structure of Al-bearing and MgSiO₃ bridgmanite at high pressure and RT, the pressure evolution of the individual B-O and A-O bond lengths, as well as the polyhedral volumes, can be derived. It has been suggested that the compression behavior of bridgmanite is mainly determined by the compressibility of B site octahedra and by the distortion of the octahedral framework (Huang, Boffa Ballaran, McCammon, Miyajima, & Frost, 2021). To describe the compression behavior of the octahedral volume V^B (Figure 2) and interatomic distances B-O (Figure S4 in Supporting Information S1), we use BM3 EOSs (1) and (2) respectively. The obtained fit parameters (Table S5 in Supporting Information S1) can be used to quantitatively describe the influence of the Si-Al substitution on the B site volume, as well as on the compressibility in bridgmanite solid solutions, and to compare them, when possible, with previous studies. Structural refinements at ambient conditions of Al-bearing bridgmanite from this study, as well as of MgSiO₃ and Fe,Al-bearing bridgmanite (Huang, Boffa Ballaran, McCammon, Miyajima, & Frost, 2021), showed that the B-O1 (apical) is longer than the two B-O2 (equatorial) distances. At high-pressure, however, the B-O1 bond shrinks more rapidly than the two B-O2 distances in all samples (Figure S4 in Supporting Information S1), which causes the octahedral distortion to progressively decrease. We observe that the overall B-O compression anisotropy of the four samples considered in our analysis is relatively similar (Figure S4 in Supporting Information S1), although the SiO₆ octahedra in

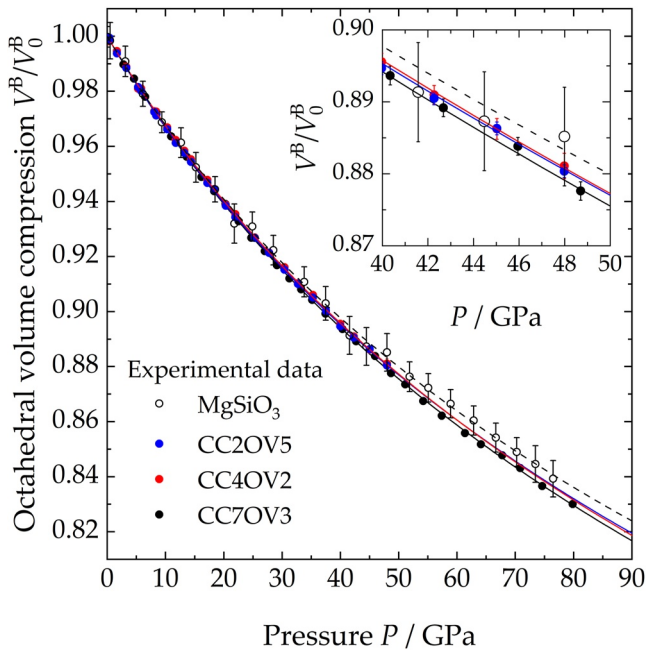


Figure 2. Compression behavior of the octahedral volume (V^B) in MgSiO_3 (empty symbols) and Al-bearing (solid symbols) bridgmanite. A BM3 equations of state was fitted to each data set and is shown as a dashed (MgSiO_3) or solid line (Al-bearing). When not shown, error bars are smaller than the symbols. In the inset, a magnification of the range between 40 and 50 GPa is shown for clarity.

MgSiO_3 bridgmanite appear to be less compressible than the $(\text{Si,Al})\text{O}_6$ octahedra of the more Al-rich bridgmanites (Figure 2). The CC7OV3 sample, which has the highest B site Al content, has the most compressible octahedra, while the octahedra of the CC2OV5 and CC4OV2 samples have very similar moduli (Table S5 in Supporting Information S1). This observation is consistent with Al-bearing samples being slightly more compressible than the end-member MgSiO_3 bridgmanite (Figure 1, Figure S3 in Supporting Information S1) and supports the idea that a tight relation exists between octahedral and bulk compressibility of perovskite structures. The variation of the octahedral incompressibility K_0^B with the octahedral volume V_0^B (Figure 3a) suggests that the OV substitution may give rise to a very slightly more compressible octahedron than the CC substitution in agreement with computational results (Brodholt, 2000). However, given the uncertainties, K_0^B of all Al-bearing samples can be described with just a linear dependency on both V_0^B and the Al content at the B site (Figure 3). If the K_0^B value for MgSiO_3 bridgmanite is taken from the BM3 fit with refined K_0^B (Table S5 in Supporting Information S1), the trends found in Figures 3a and 3b (solid lines) have relatively gentle slopes as well as high uncertainties, mainly due to the large error bar on the MgSiO_3 K_0^B value itself. However, when K_0^B is fixed to a similar value as those obtained for the Al-bearing samples (Table S5 in Supporting Information S1), the refined MgSiO_3 K_0^B helps defining a much clearer decreasing trend as a function of both V_0^B and the Al content at the B site (Figure 3, dashed lines). Although the effect of oxygen vacancies on K_0^B , and thus on K_{T0} , of Al-bearing bridgmanite seems not to be significant in our samples, it is likely to become more prominent at higher OV component contents, where higher defect concentrations can lead to the ordering and clustering of oxygen vacancies (Grüniger et al., 2019), as occurs in the brownmillerite-type structure (Brodholt, 2000). Such high OV contents are,

however, unlikely to match the composition of bridgmanite in a pyrolytic phase assemblage at topmost lower mantle conditions (Huang, Boffa Ballaran, McCammon, Miyajima, Dolejš, et al., 2021).

The A site volume (V^{A12}), defined as $V^{A12} = V/4 - V^B$ (Huang, Boffa Ballaran, McCammon, Miyajima, & Frost, 2021; Martin et al., 2006), depends mainly on the volume of the B site and on the tilting of the octahedral

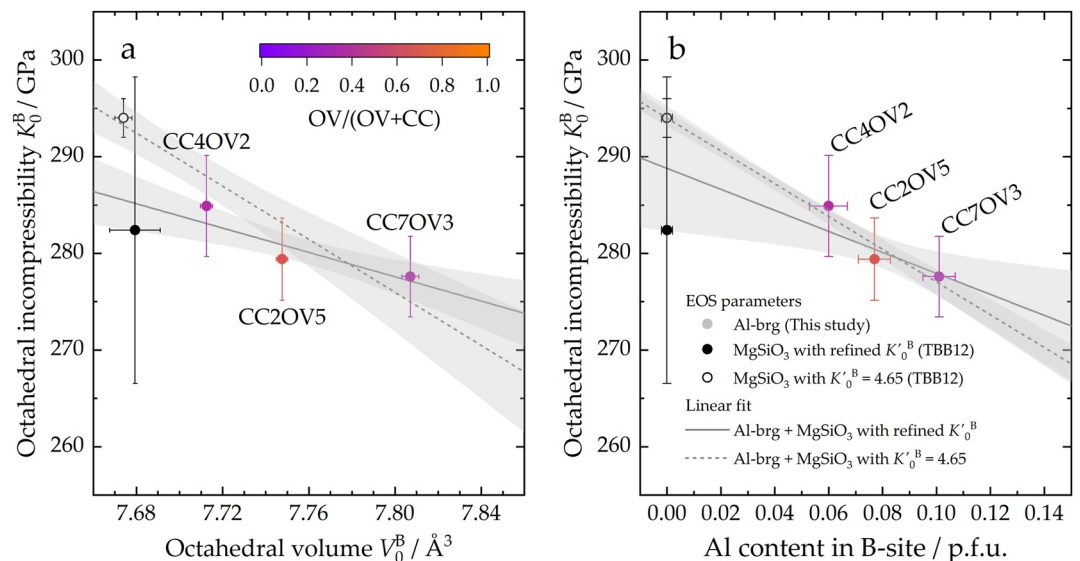


Figure 3. Octahedral incompressibility of MgSiO_3 and Al-bearing bridgmanite as a function of (a) the octahedral volume and (b) the Al content in the B site. The color scale indicates the fraction of OV component. Linear fits and their 68% confidence intervals are represented by the gray lines and shaded areas, respectively.

framework. In fact the room-pressure V_0^{A12} increases with increasing Al content (Figure S5 in Supporting Information S1) in spite of the A site substitution of Mg^{2+} by Al^{3+} , which has a much smaller ionic radius (Shannon, 1976). The same trend is observed for Fe,Al-bearing bridgmanites (Huang, Boffa Ballaran, McCammon, Miyajima, & Frost, 2021), although the latter samples have a more pronounced slope (Figure S5 in Supporting Information S1). Since Fe^{3+} has a larger ionic radius than Al^{3+} , the slightly different slopes between the Fe-bearing and Fe-free trends may indicate that the size of the A site cation has only a limited effect on V_0^{A12} and is less prominent than that of Al-Si substitution in the B site. Note also that the refined A site incompressibility values (K_0^{A12}) are found to decrease linearly as a function of both V_0^{A12} and the Al content in the B site (Figure S6 in Supporting Information S1), although Al^{3+} , being smaller than Mg^{2+} , would be generally expected to make the MgO_{12} polyhedra smaller and less compressible. Moreover, the ratio between polyhedral moduli K_0^{A12}/K_0^B for $MgSiO_3$ and Al-bearing bridgmanite ranges between 0.85(2) and 0.87(5) (Table S5 in Supporting Information S1). These values are identical within uncertainties and show no obvious systematic change as a function of composition (Figure S7 in Supporting Information S1), suggesting that Al incorporation in the B site similarly decreases both K_0^{A12} and K_0^B . As Al is incorporated at the B site of bridgmanite through both the CC and OV substitution mechanisms, their effect on the compressibility of bridgmanite seems to be indistinguishable in the compositional range investigated in this study, which is that relevant to a pyrolytic lower mantle. Therefore, it seems that oxygen vacancy concentrations relevant to pyrolytic mantle do not greatly affect the polyhedral and bulk compression behavior of bridgmanite.

4. Thermal Equation of State of Bridgmanite

To determine the thermal EOS of Al-bearing bridgmanite, pressure-volume-temperature (*PVT*) data were collected over four runs between 0 and 35 GPa and up to 1,000 K (Figure 4). As described above, in each run a crystal of CC2OV5 and one of CC4OV2 were loaded in the same pressure chamber so that a direct comparison could be made between samples with the same bulk Al content but different degrees of CC and OV substitution. We employed the thermal equation of state formalism proposed by Stixrude and Lithgow-Bertelloni (2005), which is based on a Debye model where the Debye temperature (θ_D), the Grüneisen parameter (γ), and its logarithmic derivative (q) are expressed as functions of the Eulerian finite strain (see Text S2 in Supporting Information S1). Note that a meaningful comparison between the thermoelastic parameters of $MgSiO_3$ and Al-bearing bridgmanite can be made only if consistent pressure scales are used to fit all data sets. Therefore, we first derived a best-fit thermal EOS of $MgSiO_3$ bridgmanite by reanalyzing published data using pressure scales that are consistent with one another (Text S3 in Supporting Information S1). As the fit parameters θ_{D0} , γ_0 , and q_0 (i.e., the room-pressure RT values of θ_D , γ , and q) are typically highly correlated, we then employed the θ_{D0} and q_0 values determined for $MgSiO_3$ bridgmanite in the fit of the thermal EOSs of Al-bearing bridgmanite. The refined fit parameters V_0 , K_{T0} , K'_{T0} , and γ_0 are reported in Table 4. For comparison, we also used a conventional Mie-Grüneisen-Debye (MGD) formalism (see Text S2 and S3 in Supporting Information S1) to fit the $MgSiO_3$ and Al-bearing bridgmanite *PVT* data, which yielded consistent results (Table S6, Figures S8 and S9 in Supporting Information S1). Therefore, only results from the finite-strain-based formalism of Stixrude and Lithgow-Bertelloni (2005) will be discussed here.

The γ_0 values for the CC2OV5 and CC4OV2 samples are identical within uncertainty and approximately 30% larger than γ_0 determined for $MgSiO_3$ bridgmanite by our best-fit EOS (Table 4). An attempt was made to also refine q_0 but resulted in extremely high correlation coefficients between q_0 and γ_0 , as well as in unrealistic uncertainties on q_0 (e.g., $q_0 = 1 \pm 6$) and no visible increase in the quality of the fit. Although the quality of the fit is not strongly dependent on the absolute value of q_0 , it is important to be able to evaluate the uncertainty of fixing q_0 when extrapolating the fitted EOS, particularly in temperature. To do so, we calculated isotherms using the fit parameters reported in Table 4 and varying q_0 by ± 1 (Figure S10 in Supporting Information S1). The resulting change in thermal pressure at 2000 K is approximately ± 0.5 and ± 1.5 GPa at 20 and 50 GPa, respectively (Figure S10 in Supporting Information S1). Note, however, that γ_0 and q_0 are typically highly correlated, meaning that if, for instance, q decreases as a function of Al-incorporation, then γ_0 will also be smaller than the values refined in this study. This becomes relevant, for example, if our EOSs are used to calculate the thermodynamic properties and stability of the CC end-member component at deeper lower mantle conditions, where the CC mole fraction has been argued to increase at the expense of that of the $Fe^{3+}AlO_3$ component in both pyrolytic and mid-ocean ridge basalt (Irifune et al., 2010; Ishii et al., 2022). For this purpose, further high-pressure and high-temperature measurements on CC-rich bridgmanite samples at deep lower mantle conditions will help to

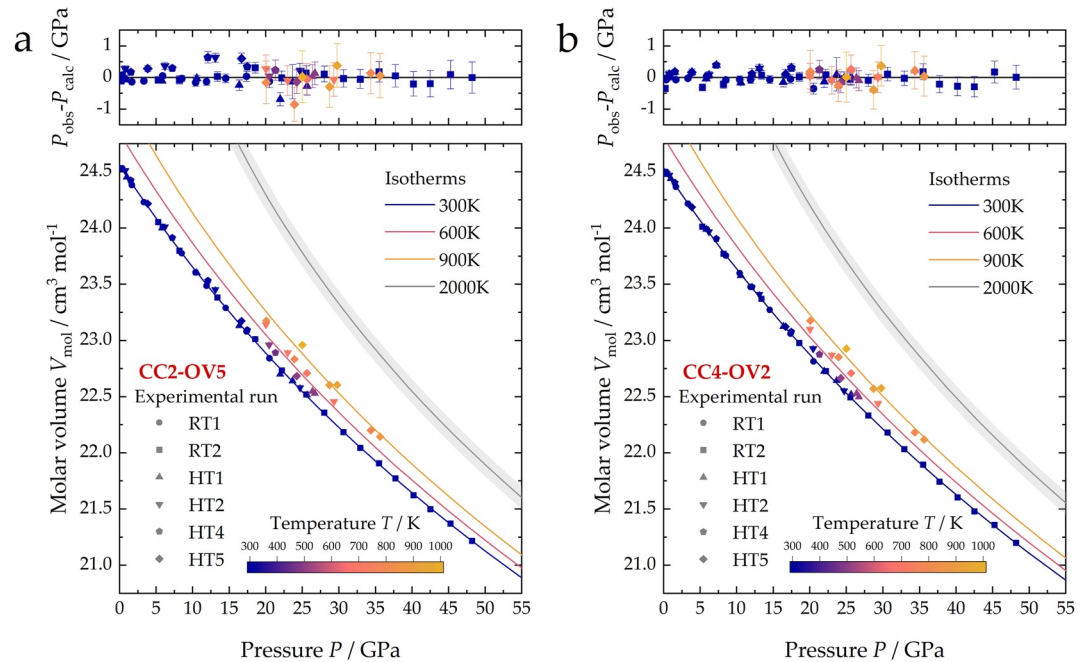


Figure 4. PVT relations of (a) CC2OV5 and (b) CC4OV2 Al-bearing bridgmanite single-crystals collected over several experimental runs. Residuals obtained from the two fits are shown above each graph. Solid lines were calculated using the finite-strain-based formalism and parameters reported in Table 4. Experimental temperatures and calculated isotherms (300–900 K) are expressed as a color scale. Additional isotherms at 2000 K (gray lines) are also plotted together with their 68% confidence intervals to show the equations of state extrapolation to temperatures relevant to the lower mantle.

more tightly constrain its thermal EOS and model the crystal chemistry and composition of bridgmanite in complex chemical systems at mid- and bottom-lower mantle conditions.

5. Solid Solution Behavior of $\text{MgSiO}_3\text{--AlAlO}_3\text{--MgAlO}_{2.5}$

Constraining the solid solution behavior of bridgmanite in the $\text{MgSiO}_3\text{--AlAlO}_3\text{--MgAlO}_{2.5}$ system is of great importance for modeling the thermodynamic and physical properties of lower mantle phase assemblages. Since the AlAlO_3 and $\text{MgAlO}_{2.5}$ bridgmanite end-members have never been synthesized, likely due to the fact that they

are not stable at any pressure/temperature conditions achieved so far, their molar volume (V_{mol}) cannot be directly constrained. Previous studies showed that non-ideality of mixing must be considered when modeling the solubility of the AlAlO_3 and $\text{MgAlO}_{2.5}$ components in $\text{MgSiO}_3\text{--bridgmanite}$ (Huang, Boffa Ballaran, McCammon, Miyajima, Dolejš, et al., 2021), if the entire $\text{MgSiO}_3\text{--AlAlO}_3$ and $\text{MgSiO}_3\text{--MgAlO}_{2.5}$ compositional ranges are considered. However, a linear dependency of volume on composition can still be safely assumed by selecting “fictive” end-member compositions for the CC and OV solid solutions that are close to the experimentally measured solubilities of the two components (i.e., ~6 mol.% $\text{MgAlO}_{2.5}$ and ~30 mol.% AlAlO_3) as suggested by the available experimental data (Figure 5a). Experimental data from this and previous studies (Daniel et al., 2004; Huang, Boffa Ballaran, McCammon, Miyajima, & Frost, 2021; Jackson et al., 2005; Kojitani et al., 2007; Z. Liu, Akaogi, et al., 2019; Z. Liu, Boffa Ballaran, et al., 2019; Z. Liu, Nishi, et al., 2017; Walter et al., 2004, 2006) for which the unit-cell or molar volume and the CC and OV contents were reported (Figure 5a), were first fitted using a three end-member linear model (i.e., $\text{MgSiO}_3\text{--AlAlO}_3\text{--MgAlO}_{2.5}$) according to:

$$V_{\text{mol}} = \sum_i n_i V_i \quad (3)$$

Table 4

Thermal Equations of State Fit Parameters for MgSiO_3 (Best-Fit) and Al-Bearing Bridgmanite (This Study) Using the Finite Strain-Based Formalism of Stixrude and Lithgow-Bertelloni (2005)

	MgSiO_3 best-fit	CC4OV2	CC2OV5
P scale	MgO^a , ruby ^b	Au^a , ruby ^b	Au^a , ruby ^b
V_{mol0} (cm^3/mol)	24.455(8)	24.536(3)	24.562(4)
T_0 (K)	298	298	298
K_{T0} (GPa)	251(2)	248.9(1.3)	246(2)
K'_{T0}	4.08(5)	3.84(7)	3.97(9)
γ_0	1.64(3)	2.12(12)	2.21(14)
q_0	3.1(2)	3.1	3.1
θ_{D0} (K)	912	912	912
n	5	5	5
reduced χ^2	1.56	2.86	3.47

Note. Numbers in italics were fixed during the fitting procedure.

^aDorogokupets and Dewaele (2007). ^bJacobsen et al. (2008).

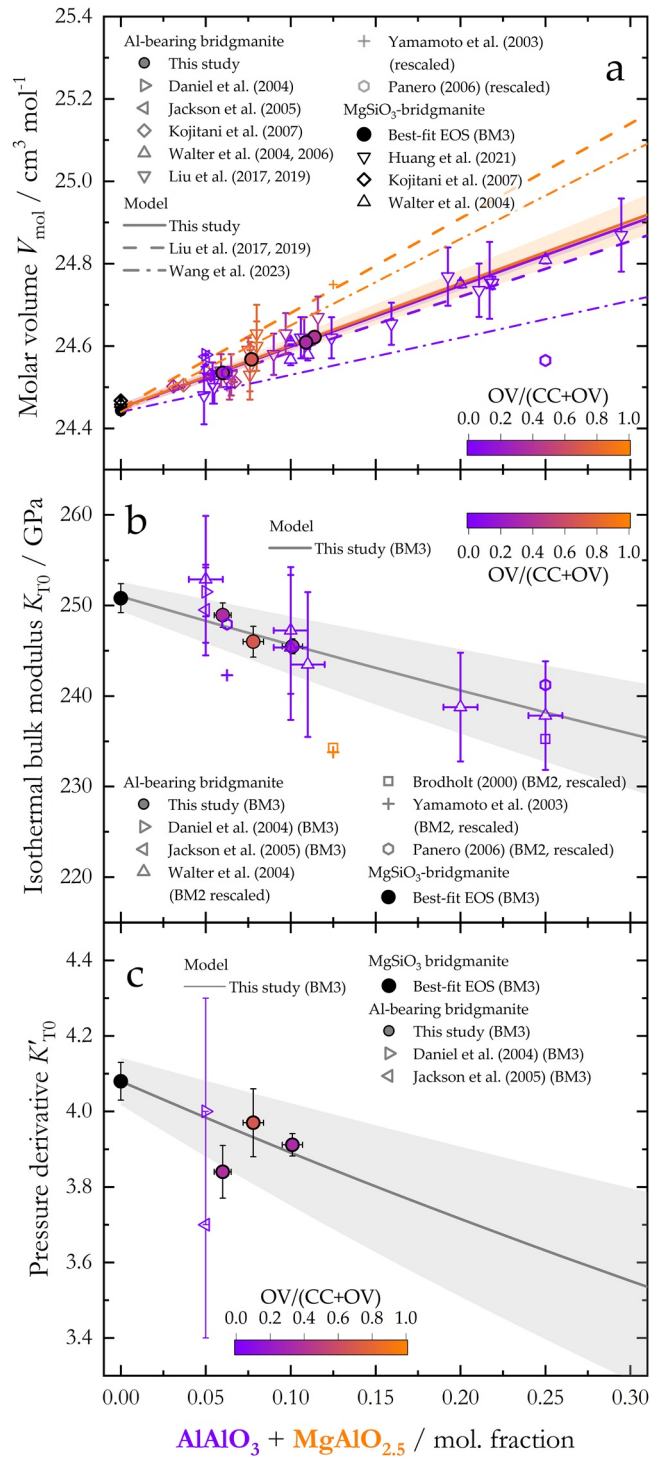


Figure 5. The compositional dependence of (a) molar volume (V_{mol}), (b) isothermal bulk modulus (K_{T0}), and (c) its pressure derivative (K'_{T0}) for Al-bearing bridgmanite at room pressure and temperature. The color scale indicates the degree of CC and OV substitution for each sample and trendline. In (a), solid lines and shaded areas indicate trends and estimated uncertainties for MgSiO₃-AlAlO₃ and MgSiO₃-MgAlO_{2.5} solid solutions determined in this study, while dashed and dot-dashed lines are trends proposed in previous studies. In (b) and (c), lines and shaded areas indicate trends and estimated uncertainties for MgSiO₃-AlAlO₃ and MgSiO₃-MgAlO_{2.5} solid solutions, under the assumption that $K_{\text{AlAlO}_3} = K_{\text{MgAlO}_{2.5}}$ and $K'_{\text{AlAlO}_3} = K'_{\text{MgAlO}_{2.5}}$.

Table 5
Modeled Equation of State Parameters for the Bridgmanite End-Members in the $MgSiO_3$ - $AlAlO_3$ - $MgAlO_{2.5}$ System

	Best-fit EOS	Refined end-members		End-members for thermodynamic modeling	
	$MgSiO_3$	$AlAlO_3$	$MgAlO_{2.5}$	$(Mg_{3/4}Al_{1/4})(Al_{1/4}Si_{3/4})O_2O_1$ CC	$Mg(Al_{1/8}Si_{7/8})O_2O_{15/16}$ OV
V_0 ($cm^3 mol^{-1}$)	24.455(8)	25.93(4)	25.96(15)	24.82(1)	24.64(2)
K_{T0} (GPa) - BM3	251(2)	208(11)	208(11)	238(5)	244(4)
K'_{T0} - BM3	4.08(5)	2.7(4)	2.7(4)	3.6(2)	3.85(15)
K_{T0} (GPa) - BM2	251.6(5)	190(3)	190(3)	231.9(17)	241.3(11)
γ_0	1.63(3)	–	–	2.1(1)	2.1(1)
q_0	3.1(2)	–	–	3.1[#]	3.1[#]
θ_{D0} (K)	912 [#]	–	–	912[#]	912[#]

Note. Refined end-member values for $AlAlO_3$ and $MgAlO_{2.5}$ were obtained by fitting data from this and previous studies using Equations 3–5. The equation of state parameters for $(Mg_{3/4}Al_{1/4})(Al_{1/4}Si_{3/4})O_2O_1$ and $Mg(Al_{1/8}Si_{7/8})O_2O_{15/16}$ were then calculated using Equations 3–5 (italics). Numbers between brackets are one standard deviation on the last digit(s). Bold values were assumed to be the same as CC4OV2 and CC2OV5 (Table 4). Hash symbols indicate values that were fixed during the fitting procedure and for which uncertainties cannot be directly evaluated.

where n_i is the molar fraction of component i in the solid solution and V_i is its molar volume, simultaneously refining V_{MgSiO_3} , V_{AlAlO_3} and $V_{MgAlO_{2.5}}$. Then, we calculated the molar volumes of 25 mol.% $AlAlO_3$ -75 mol.% $MgSiO_3$ [that is, $(Mg_{3/4}Al_{1/4})(Al_{1/4}Si_{3/4})O_3$ (CC)] and of 12.5 mol.% $MgAlO_{2.5}$ -87.5 mol.% $MgSiO_3$ [that is, $Mg(Al_{1/8}Si_{7/8})O_2O_{15/16}$ (OV)] “fictive” end-members. From our analysis, we found V_{AlAlO_3} and $V_{MgAlO_{2.5}}$ to be similar to each other within uncertainty (Table 5), which is different to the findings of Z. Liu, Boffa Ballaran, et al. (2019) and Wang et al. (2023) who proposed that $V_{MgAlO_{2.5}} > V_{AlAlO_3}$ by linearly fitting data for $MgSiO_3$ - $AlAlO_3$ solid solutions, and then fixing the obtained V_{MgSiO_3} and V_{AlAlO_3} to constrain $V_{MgAlO_{2.5}}$ from the analysis of OV-bearing samples. This neglects the potential correlation between V_{AlAlO_3} and $V_{MgAlO_{2.5}}$. Our findings support the idea that, at least for small concentrations of OV component, the molar volume of bridgmanite is mainly controlled by substitution of Al in the B site, due to its greater influence on the octahedral volume than the creation of oxygen vacancies themselves or the Mg–Al substitution in the A site.

Experimental studies on the compressibility of Al-bearing bridgmanite conducted so far have only employed powdered samples, often synthesized in situ inside a DAC (Andrault et al., 2001; Daniel et al., 2001; Walter et al., 2004, 2006). The range of values obtained for K_{T0} and K'_{T0} of these samples is considerably large, and results are often in contrast with one another. For instance, Andrault et al. (2001) and Walter et al. (2004, 2006) conducted similar experiments to determine the compressibility of bridgmanite solid solutions with different Al content, where samples were synthesized in the DAC by laser heating and their EOSs were measured upon further compression or decompression. While Andrault et al. (2001) argued that K_{T0} increases from the $MgSiO_3$ toward the $AlAlO_3$ end-member, Walter et al. (2004, 2006) reported the opposite trend, with K_{T0} linearly decreasing with increasing CC substitution. Other studies reported K_{T0} values as low as 240 and 220 GPa for bridgmanite samples with $AlAlO_3$ concentrations of 1.2 and 7.7 mol.%, respectively, which seem unrealistically low given the relatively small difference in chemical composition with the $MgSiO_3$ end-member (Daniel et al., 2001; Yagi et al., 2004). Such low K_{T0} values were argued to be related to the presence of oxygen vacancies in the investigated bridgmanite samples. However, our data indicate that the effect of oxygen vacancies is not significantly different from that of $AlAlO_3$ substitution, even for concentrations of $MgAlO_{2.5}$ as high as 5 mol.%. The broad disagreement between previous experimental studies prevents us from considering all literature data to refine K_{AlAlO_3} and $K_{MgAlO_{2.5}}$. In view of these considerations, we have fitted our single-crystal data to derive end-member properties, following the approach of Stixrude and Lithgow-Bertelloni (2011), where the solid solution behavior of K_{T0} and K'_{T0} , respectively were described, under hydrostatic stress conditions (Reuss bound), by differentiating once and twice with respect to pressure both sides of Equation 3, that is:

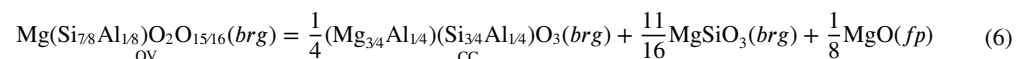
$$\frac{V_{mol}}{K_{T0}} = \sum_i n_i \frac{V_i}{K_i} \quad (4)$$

$$\frac{V_{mol}(1 + K'_{T0})}{K_{T0}^2} = \sum_i n_i \frac{V_i(1 + K'_i)}{K_i^2} \quad (5)$$

where K_i and K'_i are the ambient-pressure bulk modulus and pressure derivative of the end-member component i . As the bulk compressibility of Al-bearing bridgmanite seems to be controlled mainly by the compression of octahedra, at least for limited amounts of OV component (see Section 3.2), we constrained K_{AlAlO_3} and $K_{\text{MgAlO}_{2.5}}$, as well as K'_{AlAlO_3} and $K'_{\text{MgAlO}_{2.5}}$, to be equal to each other in the fitting procedure. To reduce the number of parameters, we fixed K_{MgSiO_3} and K'_{MgSiO_3} to the value obtained from our best-fit EOS (Table 4). In this way, we obtained $K_{\text{AlAlO}_3} = K_{\text{MgAlO}_{2.5}} = 208(11)$ GPa and $K'_{\text{AlAlO}_3} = K'_{\text{MgAlO}_{2.5}} = 2.7(4)$ based on BM3 fit parameters, and $K_{\text{AlAlO}_3} = K_{\text{MgAlO}_{2.5}} = 190(3)$ GPa based on BM2 fit parameters. Results of the molar volume and BM3 fits are plotted in Figure 5 together with 68% confidence bands (i.e., one standard deviation) represented by shaded areas. The solid solution model constructed using the BM3 EOS parameters interpolates well the refined K_{T0} data points from this study. The trend is also in good agreement with experimental data for a 5 mol.% AlAlO₃-bearing sample that was analyzed by both powder X-ray diffraction and Brillouin scattering up to approximately 40 GPa (Daniel et al., 2004; Jackson et al., 2005). The K_{T0} data from Walter et al. (2004, 2006) also show a decreasing trend with increasing Al content, despite being shifted toward significantly higher values, including the MgSiO₃ sample. If K_{T0} values are normalized to the K_{MgSiO_3} used by Walter et al. (2004) and then multiplied by K_{MgSiO_3} from our best-fit EOS, a good agreement with our data is found. Following the same approach, a good agreement with our model is also found for the rescaled K_{T0} value of OV-free Al-bearing bridgmanite from the computational studies of Brodholt (2000) and Panero et al. (2006). To compare our trends with the results of Brodholt (2000) on MgAlO_{2.5}, we show in Figure 5b the bulk modulus (calculated through Equation 4) for a solid solution of 87.5 mol.% MgSiO₃–12.5 mol.% MgAlO_{2.5}, that has the composition of the “fictive” end-member that we will later use for thermodynamic modeling. The resulting K value plots 14 GPa below our trend and 7 GPa below the lower confidence band. Again, this could either be an effect of non-ideality in the MgSiO₃–MgAlO_{2.5} system at higher MgAlO_{2.5} content or could result from the ordered oxygen vacancy distribution in the brownmillerite-type structure employed by Brodholt (2000). Yamamoto et al. (2003) also determined the bulk modulus of bridgmanite solid solutions with 6.25 mol.% CC and 12.5 mol.% OV compositions by means of first-principle calculations. Their results suggest that K_{T0} decreases in a similar fashion with increasing CC and OV contents (Figure 5b), although with a more pronounced slope with respect to the trend proposed in our study. Similar considerations apply to the BM2 K_{T0} which are reported in the Supporting Information (Figure S11 in Supporting Information S1). K'_{T0} values for the BM3 solid solution model are in slightly poorer agreement due to the relatively low refined value for CC4OV2 (Table 3), but still consistent with the refined model within mutual uncertainties.

6. Implications for the Stability of the Oxygen Vacancy Component in Al-Bearing Bridgmanite

The presence of defects in the crystal structure of lower mantle minerals has the potential to greatly affect the transport properties of lower mantle rocks, such as their viscosity. For instance, the pressure dependence of defects could contribute to enhance mantle viscosity at depths greater than 1,000 km (Rudolph et al., 2015), which in turn has been linked to slab stagnation (Fukao & Obayashi, 2013) and plume deflection (French & Romanowicz, 2015) in the same depth interval. This has motivated a number of previous studies to investigate and model the stability of the bridgmanite OV components MgAlO_{2.5} and MgFe³⁺O_{2.5} as a function of pressure (H. Fei et al., 2021; Huang, Boffa Ballaran, McCammon, Miyajima, Dolejš, et al., 2021; Z. Liu, Ishii, et al., 2017). The main limitation of the models proposed so far is that the thermoelastic parameters of the AlAlO₃ and MgAlO_{2.5} bridgmanite end-members, which are required to model the stability of oxygen vacancies as a function of pressure, were assumed to be equal to MgSiO₃ or derived from crystallographic observations at ambient conditions (Huang, Boffa Ballaran, McCammon, Miyajima, Dolejš, et al., 2021; Huang, Boffa Ballaran, McCammon, Miyajima, & Frost, 2021). Here, we have combined the thermodynamic formalism proposed in these previous studies with the thermal equation of state parameters for MgSiO₃ and Al-bearing bridgmanite end-members determined in this study (Table 5). In order to model the stability of oxygen vacancies in bridgmanite in the MgO–AlO_{1.5}–SiO₂ system, we assumed the following equilibrium:



where *brg* and *fp* indicate components of bridgmanite and ferropericlase, respectively. Note that the AlAlO₃ and MgAlO_{2.5} end-member components have been replaced by the “fictive” end-members with intermediate compositions introduced in the previous section, which will be referred to as CC and OV hereinafter, in order to limit the

extent to which the experimental data are extrapolated and minimize potential non-ideal effects. The equilibrium constant for the reaction (6) is related to the standard state (pure phases at the pressure and temperature of interest) Gibbs free energy change (ΔG^0) by:

$$\Delta G^0 = -RT \ln \frac{\left(a_{\text{CC}}^{\text{brg}}\right)^{\frac{1}{4}} \left(a_{\text{MgSiO}_3}^{\text{brg}}\right)^{\frac{11}{16}} \left(a_{\text{MgO}}^{\text{fp}}\right)^{\frac{1}{8}}}{a_{\text{OV}}^{\text{brg}}} \quad (7)$$

where a_i^α is the activity of the component i in the phase α , R is the gas constant and T is temperature. The activity of the component i in the phase α is calculated as $a_i^\alpha = x_i^\alpha \gamma_i^\alpha$, where x is the ideal mixing activity and γ is the activity coefficient accounting for non-ideal mixing. In the MgO–AlO_{1.5}–SiO₂ system, ferropericlae is pure MgO and, thus, its activity is 1. Following Huang, Boffa Ballaran, McCammon, Miyajima, Dolejš, et al. (2021), we arbitrarily assumed the oxygen vacancies to be localized in the O1 site of bridgmanite. Previous density functional theory (DFT) calculations proposed MgAlO_{2.5} with a brownmillerite-type structure to be the OV end-member of bridgmanite (Brodholt, 2000), with oxygen vacancies being ordered and localized at the O2 site in alternate layers perpendicular to the c -axis. In this structural type, Al occupies either tetrahedral or octahedral sites, while recent ²⁷Al magic-angle spinning nuclear magnetic resonance (MAS NMR) showed evidence also for 5-fold coordinated Al (Grüniger et al., 2019), which is in principle compatible with both O1 and O2 vacancies. However, as we will discuss later, the choice of the specific site where oxygen vacancies are located does not affect our thermodynamic model as the dominant interaction parameter in the nearest-neighbor model is related to Si–Al substitution in the B site. Under these assumptions, the ideal mixing activity of bridgmanite components is calculated as follows:

$$x_{\text{MgSiO}_3}^{\text{brg}} = \left(x_{\text{Mg}}^{\text{A}}\right) \left(x_{\text{Si}}^{\text{B}}\right) \left(x_{\text{O}}^{\text{O1}}\right) \quad (8)$$

$$x_{\text{CC}}^{\text{brg}} = 3.0792 \left(x_{\text{Mg}}^{\text{A}}\right)^{\frac{3}{4}} \left(x_{\text{Al}}^{\text{A}}\right)^{\frac{1}{4}} \left(x_{\text{Si}}^{\text{B}}\right)^{\frac{3}{4}} \left(x_{\text{Al}}^{\text{B}}\right)^{\frac{1}{4}} \left(x_{\text{O}}^{\text{O1}}\right) \quad (9)$$

$$x_{\text{OV}}^{\text{brg}} = 1.8415 \left(x_{\text{Mg}}^{\text{A}}\right) \left(x_{\text{Si}}^{\text{B}}\right)^{\frac{7}{8}} \left(x_{\text{Al}}^{\text{B}}\right)^{\frac{1}{8}} \left(x_{\text{O}}^{\text{O1}}\right)^{\frac{15}{16}} \left(x_{\text{V}}^{\text{O1}}\right)^{\frac{1}{16}} \quad (10)$$

where x is the concentration of Mg, Si, Al, O or vacancies (V) in the A, B or O1 crystallographic site of the bridgmanite structure. The normalization constants 3.0792 and 1.8415 are required in order for the end-member activity of the (Mg_{3/4}Al_{1/4})(Al_{1/4}Si_{3/4})O₂O₁ and Mg(Al_{1/8}Si_{7/8})O₂O_{15/16} bridgmanite components to be 1 (see Text S4 in Supporting Informaton S1). The activity coefficients for non-ideal mixing are calculated assuming a nearest-neighbor binary symmetric model:

$$RT \ln \gamma_{\text{CC}}^{\text{brg}} = W_{\text{MgAl}}^{\text{A}} \left(1 - x_{\text{Al}}^{\text{A}}\right)^2 + W_{\text{AlSi}}^{\text{B}} \left(1 - x_{\text{Al}}^{\text{B}}\right)^2 + W_{\text{OV}}^{\text{O1}} \left(1 - x_{\text{O}}^{\text{O1}}\right)^2 \quad (11)$$

$$RT \ln \gamma_{\text{MgSiO}_3}^{\text{brg}} = W_{\text{MgAl}}^{\text{A}} \left(1 - x_{\text{Mg}}^{\text{A}}\right)^2 + W_{\text{AlSi}}^{\text{B}} \left(1 - x_{\text{Si}}^{\text{B}}\right)^2 + W_{\text{OV}}^{\text{O1}} \left(1 - x_{\text{O}}^{\text{O1}}\right)^2 \quad (12)$$

$$RT \ln \gamma_{\text{OV}}^{\text{brg}} = W_{\text{MgAl}}^{\text{A}} \left(1 - x_{\text{Mg}}^{\text{A}}\right)^2 + W_{\text{AlSi}}^{\text{B}} \left(1 - x_{\text{Al}}^{\text{B}}\right)^2 + W_{\text{OV}}^{\text{O1}} \left(1 - x_{\text{V}}^{\text{O1}}\right)^2 \quad (13)$$

where W are Margules interaction parameters describing the interaction of Mg–Al in the A site, Al–Si in the B site or O–V in the O1 site. By assuming $W_{\text{MgAl}}^{\text{B}} = W_{\text{OV}}^{\text{O1}} = 0$ (Huang, Boffa Ballaran, McCammon, Miyajima, Dolejš, et al., 2021) and substituting Equations 8–13, we can rewrite Equation 7 explicitly as a function of composition:

$$\Delta G^0 = -RT \ln \frac{\left(x_{\text{CC}}^{\text{brg}}\right)^{\frac{1}{4}} \left(x_{\text{MgSiO}_3}^{\text{brg}}\right)^{\frac{11}{16}}}{\left(x_{\text{OV}}^{\text{brg}}\right)} - W_{\text{AlSi}}^{\text{B}} \left[\frac{1}{4} \left(x_{\text{Si}}^{\text{B}}\right)^2 + \frac{11}{16} \left(x_{\text{Al}}^{\text{B}}\right)^2 - \left(x_{\text{Si}}^{\text{B}}\right)^2 \right] \quad (14)$$

Equivalent expressions were also calculated assuming the dominant interaction parameter to be $W_{\text{MgAl}}^{\text{B}}$ or $W_{\text{OV}}^{\text{O1}}$. However, the fit did not reach convergence in these cases, supporting the choice of $W_{\text{AlSi}}^{\text{B}}$ as the most relevant interaction parameter.

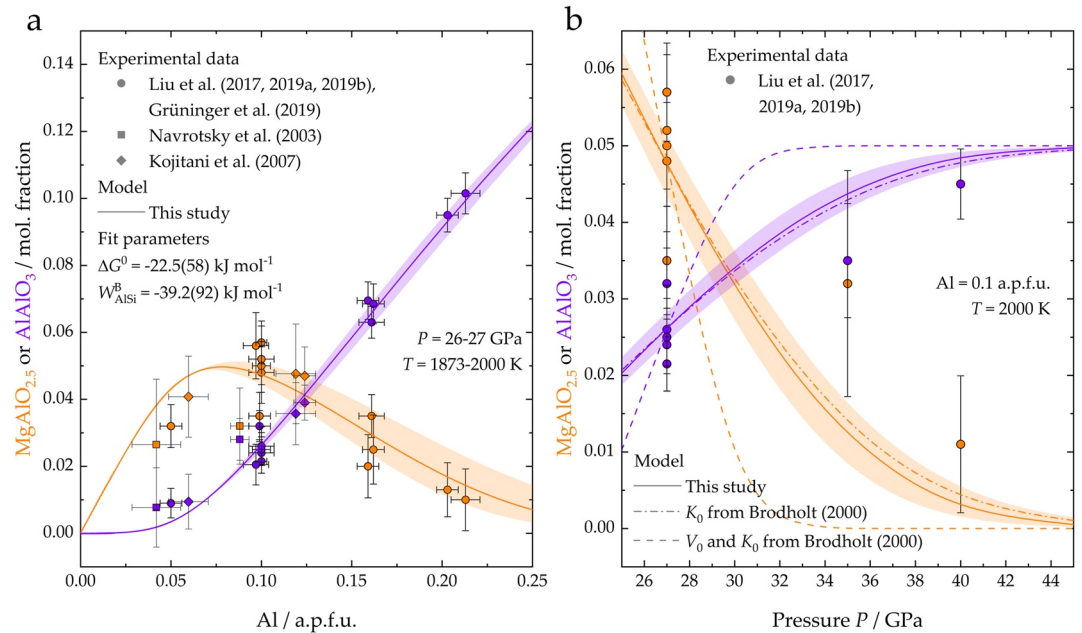


Figure 6. Concentration of AlAlO₃ (CC) and MgAlO_{2.5} (OV) components in bridgmanite (a) as a function of the bulk Al content at 27 GPa and 2,000 K, and (b) as a function of pressure at 0.1 Al a.p.f.u. and 2,000 K (Z. Liu, Akaogi, et al., 2019; Z. Liu, Boffa Ballaran, et al., 2019; Z. Liu, Ishii, et al., 2017). In (a), results from experiments conducted at 1,873 K and 27 GPa (Kojitani et al., 2007) and 26 GPa (Navrotsky et al., 2003) are also reported for comparison. The shaded areas indicate the estimated uncertainties and take into account (a, b) the correlation between ΔG^0 and W_{AlSi}^B (Figure S12 in Supporting Information S1) and (b) the uncertainty on the equation of state parameters (Table 5).

Since most of the experimental studies on the phase relations of OV-bearing bridgmanite in the MgO–SiO₂–AlO_{1.5} system were conducted at 26–27 GPa and 1,873–2,000 K (Grüniger et al., 2019; Kojitani et al., 2007; Z. Liu, Akaogi, et al., 2019; Z. Liu, Boffa Ballaran, et al., 2019; Navrotsky et al., 2003), we assumed 27 GPa and 2000 K as standard state conditions in our calculations. We used OriginPro 2021 (OriginLab corporation, Northampton, MA, USA) to fit the compositional data for bridgmanite synthesized under MgO-saturated conditions. The analytical uncertainties on EPMA data were propagated to the fit parameters ΔG^0 and W_{AlSi}^B using an orthogonal regression scheme. The obtained model fits the experimental data points well (Figure 6a). From our fit, we found $\Delta G^0 = -22(6) \text{ kJ mol}^{-1}$ and $W_{\text{AlSi}}^B = -39(9) \text{ kJ mol}^{-1}$, which are in agreement with previous results within mutual uncertainties (Huang, Boffa Ballaran, McCammon, Miyajima, Dolejš, et al., 2021). As suggested by these authors, the correlation between the two fit parameters is extremely high (Figure S12 in Supporting Information S1), which in turn is responsible for the large estimated errors on the parameters of our fit.

Using the thermal EOS parameters for the three end-members MgSiO₃, (Mg_{3/4}Al_{1/4})(Al_{1/4}Si_{3/4})O₂O₁ (CC) and Mg(Al_{1/8}Si_{7/8})O₂O_{15/16} (OV), we can evaluate how the Gibbs free energy in Equation 14 evolves with pressure (Text S5 in Supporting Information S1) in the MgO–AlO_{1.5}–SiO₂ system under MgO saturated conditions (Figure 6b). The main factor controlling how pressure affects the OV concentration in bridgmanite is the term $P\Delta V$ (see Equation S11 in the Text S5 in Supporting Information S1). As the ΔV term for the equilibrium (6) is negative, the concentration of the OV component will decrease with increasing pressure, regardless of the fact that the OV and CC components have essentially similar end-member volumes and EOS properties. To evaluate the effect of the EOS fit parameters on the model, we added or subtracted the estimated uncertainties on V_0 , K_0 , and K'_0 for the OV and CC end-members (Table 5) in a way to maximize or minimize the ΔV term. We found the contribution to overall uncertainties on the CC and OV concentration to be much smaller than that arising from data scattering at 27 GPa and 2,000 K (Figure 6a). The experimental data of Z. Liu, Ishii, et al. (2017) at 2,000 K and 27–40 GPa exhibit a similarly decreasing trend for the concentration of the OV component, although with a slightly milder slope (Figure 6b). This difference is significant only for the data point at 35 GPa, where the experimentally determined OV concentration and that determined from our model do not overlap within one standard deviation. As this could be related to the choice of EOS parameters used to extrapolate the model to higher pressures, we further tested the sensitivity of the model to the input EOS parameters for the CC and OV end-members

by employing a combination of V_0 from this study and K_0 from Brodholt (2000). Despite the larger difference between K_{AlAlO_3} and $K_{\text{MgAlO}_{2.5}}$, the change in concentration of the two end-members as a function of pressure falls within the estimated uncertainties of our model. If both V_0 and K_0 from Brodholt (2000) are employed, owing to the much larger difference between $V_{\text{MgAlO}_{2.5}}$ and V_{AlAlO_3} , the OV concentration drops to zero already at 33 GPa, which is inconsistent with the available experimental data (Z. Liu, Ishii, et al., 2017). Alternatively, as seems to be the case for some scattered data points at 26–27 GPa and 1,873–2,000 K in Figure 6a, the misfit may simply originate from slight inaccuracies in pressure determination or chemical analyses or from an underestimation of the analytical uncertainties in the previous experimental study. The modeled OV concentration is also in good agreement with that calculated by Huang, Boffa Ballaran, McCammon, Miyajima, Dolejš, et al. (2021) who, however, assumed all bridgmanite components to have the same elastic and thermal parameters.

In the present study we determined the thermoelastic parameters of Al-bearing bridgmanite single crystals for the first time. Our RT data clearly show that both the bulk compressibility of the bridgmanite structure and the polyhedral compressibility are controlled by the Si–Al substitution in the B site rather than the concentration of oxygen vacancies. High temperature data up to 1,000 K at lower mantle pressures allowed the Grüneisen parameter to be refined with reasonable uncertainties, although the tradeoff with its volume derivative q was neglected. Direct measurements of the elastic parameters of bridgmanite at high pressure and temperature, for instance by Brillouin scattering in the DAC and ultrasonic interferometry in the multi-anvil press, would likely allow this trade off to be resolved as they are more sensitive to the thermal parameters of solids (Stixrude & Lithgow-Bertelloni, 2005). However, such measurements are also significantly more challenging from an experimental point of view, which is reflected in the scarcity of elasticity data for Al-bearing bridgmanite in the literature. Therefore, X-ray diffraction measurements presented here constitute an important step toward constraining the thermoelastic properties of Al-bridgmanite end-members which are required to model the seismic velocities and composition of bridgmanite in complex mineral physical models.

Further challenges in determining the composition of bridgmanite as a function of pressure involve the incorporation mechanism of Fe^{3+} . Huang, Boffa Ballaran, McCammon, Miyajima, Dolejš, et al. (2021) predicted that the concentration of the $\text{Fe}^{3+}\text{Fe}^{3+}\text{O}_3$ component in bridgmanite could increase with pressure and become relevant for a pyrolytic lower mantle composition. The presence of such a component could have important implications for the electronic and elastic properties of bridgmanite, as octahedrally coordinated Fe^{3+} undergoes a pressure-induced high-spin to low-spin crossover, affecting the density and seismic velocities of bridgmanite-bearing rocks (J. Liu et al., 2018; Mao et al., 2015). Recent experimental data showed that both the $\text{Fe}^{3+}\text{Fe}^{3+}\text{O}_3$ and $\text{MgFe}^{3+}\text{O}_{2.5}$ end-members are stabilized under oxidizing conditions in Al-free systems and that the concentration of the $\text{MgFe}^{3+}\text{O}_{2.5}$ component decreases with pressure (H. Fei et al., 2020, 2021). In these experiments, bridgmanite was found to coexist with a post-spinel phase of MgFe_2O_4 and/or ferroperrichite. As phase assemblages become more complex with the addition of Fe, constraining the thermal equation of state of $\text{Fe}^{3+}\text{Fe}^{3+}\text{O}_3$ -bearing and $\text{MgFe}^{3+}\text{O}_{2.5}$ -bearing bridgmanite is of crucial importance to model the phase equilibria of Fe-bearing systems, such as candidate rock compositions for the lower mantle like pyrolite and basalt. As EOSs of different components become more and more accurate, our ability to build more complete thermodynamic models will also improve, allowing us to predict the stability of bridgmanite components and calculate their physical properties over a wider pressure, temperature, and compositional range than it is currently possible.

Acknowledgments

We would like to thank Raphael Njul for preparing the samples for EPMA and Detlef Krauß for his assistance with the acquisition of EPMA data. We also thank two anonymous reviewers and the associate editor for their constructive comments that helped us improving the manuscript. This study was supported by the Deutsche Forschungsgemeinschaft (DFG) grant FR1555/11. We acknowledge the Deutsches Elektronen-Synchrotron DESY (Hamburg, Germany), a member of the Helmholtz Association HGF, for the provision of experimental facilities. Parts of this research were carried out at the Extreme Conditions Beamline P02.2, PETRA-III. Open Access funding enabled and organized by Projekt DEAL.

Data Availability Statement

Crystallographic information files of single-crystal structural refinements of MgSiO_3 and Al-bearing bridgmanite at high pressure are available at the following data repository: <https://doi.org/10.6084/m9.figshare.21618168>

References

- Andrault, D., Bolfan-Casanova, N., Bouhifd, M. A., Guignot, N., & Kawamoto, T. (2007). The role of Al-defects on the equation of state of Al-(Mg,Fe)SiO₃ perovskite. *Earth and Planetary Science Letters*, 263(3–4), 167–179. <https://doi.org/10.1016/j.epsl.2007.08.012>
- Andrault, D., Bolfan-Casanova, N., & Guignot, N. (2001). Equation of state of lower mantle (Al,Fe)-MgSiO₃ perovskite. *Earth and Planetary Science Letters*, 193(3–4), 501–508. [https://doi.org/10.1016/S0012-821X\(01\)00506-4](https://doi.org/10.1016/S0012-821X(01)00506-4)
- Angel, R. J. (2000). Equations of state. *Reviews in Mineralogy and Geochemistry*, 41(1), 35–59. <https://doi.org/10.2138/rmg.2000.41.2>
- Angel, R. J., & Finger, L. W. (2011). SINGLE: A program to control single-crystal diffractometers. *Journal of Applied Crystallography*, 44(1), 247–251. <https://doi.org/10.1107/S0021889810042305>
- Angel, R. J., Gonzalez-Platas, J., & Alvaro, M. (2014). EoSFit7c and a Fortran module (library) for equation of state calculations. *Zeitschrift Fur Kristallographie*, 229(5), 405–419. <https://doi.org/10.1515/zkri-2013-1711>

- Birch, F. (1947). Finite elastic strain of cubic crystals. *Physical Review*, 71(11), 809–824. <https://doi.org/10.1103/PhysRev.71.809>
- Boehler, R., & De Hantsetters, K. (2004). New anvil designs in diamond-cells. *High Pressure Research*, 24(3), 391–396. <https://doi.org/10.1080/08957950412331323924>
- Boffa Ballaran, T., Kurnosov, A., Glazyrin, K., Frost, D. J., Merlini, M., Hanfland, M., & Caracas, R. (2012). Effect of chemistry on the compressibility of silicate perovskite in the lower mantle. *Earth and Planetary Science Letters*, 333(3/4), 181–190. <https://doi.org/10.1016/j.epsl.2012.03.029>
- Brodholt, J. P. (2000). Pressure-induced changes in the compression mechanism of aluminous perovskite in the Earth's mantle. *Nature*, 407(6804), 620–622. <https://doi.org/10.1038/35036565>
- Criniti, G., Kurnosov, A., Boffa Ballaran, T., & Frost, D. J. (2021). Single-crystal elasticity of MgSiO₃ bridgmanite to mid-lower mantle pressure. *Journal of Geophysical Research: Solid Earth*, 126(5). <https://doi.org/10.1029/2020JB020967>
- Daniel, I., Bass, J. D., Fiquet, G., Cardon, H., Zhang, J., & Hanfland, M. (2004). Effect of aluminium on the compressibility of silicate perovskite. *Geophysical Research Letters*, 31(15), 3–6. <https://doi.org/10.1029/2004GL020213>
- Daniel, I., Cardon, H., Fiquet, G., Guyot, F., & Mezoaur, M. (2001). Equation of state of Al-bearing perovskite to lower mantle pressure conditions. *Geophysical Research Letters*, 28(19), 3789–3792. <https://doi.org/10.1029/2001gl013011>
- de Grouchy, C. J. L., Sanloup, C., Cochain, B., Drewitt, J. W. E., Kono, Y., & Crépeau, C. (2017). Lutetium incorporation in magmas at depth: Changes in melt local environment and the influence on partitioning behaviour. *Earth and Planetary Science Letters*, 464, 155–165. <https://doi.org/10.1016/j.epsl.2017.02.017>
- Dorogokupets, P. I., & Dewaele, A. (2007). Equations of state of MgO, Au, Pt, NaCl-B1, and NaCl-B2: Internally consistent high-temperature pressure scales. *High Pressure Research*, 27(4), 431–446. <https://doi.org/10.1080/08957950701659700>
- Fei, H., Liu, Z., Huang, R., Kamada, S., Hirao, N., Kawaguchi, S., et al. (2021). Pressure destabilizes oxygen vacancies in bridgmanite. *Journal of Geophysical Research: Solid Earth*, 126(12), 1–18. <https://doi.org/10.1029/2021JB022437>
- Fei, H., Liu, Z., McCammon, C., & Katsura, T. (2020). Oxygen vacancy substitution linked to ferric iron in bridgmanite at 27 GPa. *Geophysical Research Letters*, 47(6), e2019GL086296. <https://doi.org/10.1029/2019GL086296>
- Fei, Y., & Mao, H. K. (1994). In situ determination of the NiAs phase of FeO at high pressure and temperature. *Science*, 266(5191), 1678–1680. <https://doi.org/10.1126/science.266.5191.1678>
- French, S. W., & Romanowicz, B. (2015). Broad plumes rooted at the base of the Earth's mantle beneath major hotspots. *Nature*, 525(7567), 95–99. <https://doi.org/10.1038/nature14876>
- Fukao, Y., & Obayashi, M. (2013). Subducted slabs stagnant above, penetrating through, and trapped below the 660 km discontinuity. *Journal of Geophysical Research: Solid Earth*, 118(11), 5920–5938. <https://doi.org/10.1002/2013JB010466>
- Gonzalez-Platas, J., Alvaro, M., Nestola, F., & Angel, R. J. (2016). EosFit7-GUI: A new graphical user interface for equation of state calculations, analyses and teaching. *Journal of Applied Crystallography*, 49(4), 1377–1382. <https://doi.org/10.1107/S1600576716008050>
- Grüniger, H., Liu, Z., Siegel, R., Boffa Ballaran, T., Katsura, T., Senker, J., & Frost, D. J. (2019). Oxygen vacancy ordering in aluminous bridgmanite in the Earth's lower mantle. *Geophysical Research Letters*, 46(15), 8731–8740. <https://doi.org/10.1029/2019GL083613>
- Huang, R., Boffa Ballaran, T., McCammon, C. A., Miyajima, N., Dolejš, D., & Frost, D. J. (2021). The composition and redox state of bridgmanite in the lower mantle as a function of oxygen fugacity. *Geochimica et Cosmochimica Acta*, 303, 110–136. <https://doi.org/10.1016/j.gca.2021.02.036>
- Huang, R., Boffa Ballaran, T., McCammon, C. A., Miyajima, N., & Frost, D. J. (2021). The effect of Fe–Al substitution on the crystal structure of MgSiO₃ bridgmanite. *Journal of Geophysical Research: Solid Earth*, 126(9), e2021JB021936. <https://doi.org/10.1029/2021jb021936>
- Hübschle, C. B., Sheldrick, G. M., & Dittrich, B. (2011). ShelXle: A Qt graphical user interface for SHELXL. *Journal of Applied Crystallography*, 44(6), 1281–1284. <https://doi.org/10.1107/S0021889811043202>
- Irifune, T., Shinmei, T., McCammon, C. A., Miyajima, N., Rubie, D. C., & Frost, D. J. (2010). Iron partitioning and density changes of pyrolyte in Earth's lower mantle. *Science*, 327(5962), 193–195. <https://doi.org/10.1126/science.1181443>
- Ishii, T., Liu, Z., & Katsura, T. (2019). A breakthrough in pressure generation by a Kawai-type multi-anvil apparatus with tungsten carbide anvils. *Engineering*, 5(3), 434–440. <https://doi.org/10.1016/j.eng.2019.01.013>
- Ishii, T., Miyajima, N., Criniti, G., Hu, Q., Glazyrin, K., & Katsura, T. (2022). High pressure-temperature phase relations of basaltic crust up to mid-mantle conditions. *Earth and Planetary Science Letters*, 584, 117472. <https://doi.org/10.1016/j.epsl.2022.117472>
- Ishii, T., Shi, L., Huang, R., Tsujino, N., Druzhbin, D., Myhill, R., et al. (2016). Generation of pressures over 40 GPa using Kawai-type multi-anvil press with tungsten carbide anvils. *Review of Scientific Instruments*, 87(2). <https://doi.org/10.1063/1.4941716>
- Jackson, J. M., Zhang, J., Shu, J., Sinogeikin, S. V., & Bass, J. D. (2005). High-pressure sound velocities and elasticity of aluminous MgSiO₃ perovskite to 45 GPa: Implications for lateral heterogeneity in Earth's lower mantle. *Geophysical Research Letters*, 32(21), 1–4. <https://doi.org/10.1029/2005GL023522>
- Jacobsen, S. D., Holl, C. M., Adams, K. A., Fischer, R. A., Martin, E. S., Bina, C. R., et al. (2008). Compression of single-crystal magnesium oxide to 118 GPa and a ruby pressure gauge for helium pressure media. *American Mineralogist*, 93(11–12), 1823–1828. <https://doi.org/10.2138/am.2008.2988>
- Kantor, I., Prakapenka, V., Kantor, A., Dera, P., Kurnosov, A., Sinogeikin, S., et al. (2012). BX90: A new diamond anvil cell design for X-ray diffraction and optical measurements. *Review of Scientific Instruments*, 83(12), 125102. <https://doi.org/10.1063/1.4768541>
- Keppeler, H., & Frost, D. J. (2005). Introduction to minerals under extreme conditions. In *EMU notes in Mineralogy* (pp. 1–30). <https://doi.org/10.1180/emu-notes.7.1>
- King, H. E., & Finger, L. W. (1979). Diffracted beam crystal centering and its application to high-pressure crystallography. *Journal of Applied Crystallography*, 12(4), 374–378. <https://doi.org/10.1107/S0021889879012723>
- Kojitani, H., Katsura, T., & Akaogi, M. (2007). Aluminum substitution mechanisms in perovskite-type MgSiO₃: An investigation by Rietveld analysis. *Physics and Chemistry of Minerals*, 34(4), 257–267. <https://doi.org/10.1007/s00269-007-0144-z>
- Kurnosov, A., Kantor, I., Boffa-Ballaran, T., Lindhardt, S., Dubrovinsky, L., Kuznetsov, A., & Zehnder, B. H. (2008). A novel gas-loading system for mechanically closing of various types of diamond anvil cells. *Review of Scientific Instruments*, 79(4), 045110. <https://doi.org/10.1063/1.2902506>
- Kurnosov, A., Marquardt, H., Frost, D. J., Boffa Ballaran, T., & Ziberna, L. (2017). Evidence for a Fe³⁺-rich pyrolytic lower mantle from (Al,Fe)-bearing bridgmanite elasticity data. *Nature*, 543(7646), 543–546. <https://doi.org/10.1038/nature21390>
- Liermann, H. P., Konôpková, Z., Morgenroth, W., Glazyrin, K., Bednarčík, J., McBride, E. E., et al. (2015). The extreme conditions beamline P02.2 and the extreme conditions science infrastructure at PETRA III. *Journal of Synchrotron Radiation*, 22(4), 908–924. <https://doi.org/10.1107/S1600577515005937>
- Liu, J., Dorfman, S. M., Zhu, F., Li, J., Wang, Y., Zhang, D., et al. (2018). Valence and spin states of iron are invisible in Earth's lower mantle. *Nature Communications*, 9(1), 1–9. <https://doi.org/10.1038/s41467-018-03671-5>

- Liu, Z., Akaogi, M., & Katsura, T. (2019). Increase of the oxygen vacancy component in bridgmanite with temperature. *Earth and Planetary Science Letters*, 505, 141–151. <https://doi.org/10.1016/j.epsl.2018.10.014>
- Liu, Z., Boffa Ballaran, T., Huang, R., Frost, D. J., & Katsura, T. (2019). Strong correlation of oxygen vacancies in bridgmanite with Mg/Si ratio. *Earth and Planetary Science Letters*, 523, 115697. <https://doi.org/10.1016/j.epsl.2019.06.037>
- Liu, Z., Fei, H., Chen, L., McCammon, C., Wang, L., Liu, R., et al. (2021). Bridgmanite is nearly dry at the top of the lower mantle. *Earth and Planetary Science Letters*, 570, 117088. <https://doi.org/10.1016/j.epsl.2021.117088>
- Liu, Z., Ishii, T., & Katsura, T. (2017). Rapid decrease of MgAlO_{2.5} component in bridgmanite with pressure. *Geochemical Perspectives Letters*, 5, 12–18. <https://doi.org/10.7185/geochemlet.1739>
- Liu, Z., Nishi, M., Ishii, T., Fei, H., Miyajima, N., Ballaran, T. B., et al. (2017). Phase relations in the system MgSiO₃-Al₂O₃ up to 2300 K at lower mantle pressures. *Journal of Geophysical Research: Solid Earth*, 122(10), 7775–7788. <https://doi.org/10.1002/2017JB014579>
- Mao, Z., Lin, J. F., Yang, J., Inoue, T., & Prakapenka, V. B. (2015). Effects of the Fe³⁺ spin transition on the equation of state of bridgmanite. *Geophysical Research Letters*, 42(11), 4335–4342. <https://doi.org/10.1002/2015GL064400>
- Martin, C. D., Crichton, W. A., Liu, H., Prakapenka, V., Chen, J., & Parise, J. B. (2006). Rietveld structure refinement of perovskite and post-perovskite phases of NaMgF₃ (Neighborite) at high pressures. *American Mineralogist*, 91(10), 1703–1706. <https://doi.org/10.2138/am.2006.2308>
- Navrotsky, A., Schoenitz, M., Kojitani, H., Xu, H., Zhang, J., Weidner, D. J., & Jeanloz, R. (2003). Aluminum in magnesium silicate perovskite: Formation, structure, and energetics of magnesium-rich defect solid solutions. *Journal of Geophysical Research*, 108(B7). <https://doi.org/10.1029/2002jb002055>
- Pamato, M. G., Kurnosov, A., Boffa Ballaran, T., Frost, D. J., Ziberna, L., Giannini, M., et al. (2016). Single crystal elasticity of majoritic garnets: Stagnant slabs and thermal anomalies at the base of the transition zone. *Earth and Planetary Science Letters*, 451, 114–124. <https://doi.org/10.1016/j.epsl.2016.07.019>
- Panero, W. R., Akber-Knutson, S., & Stixrude, L. (2006). Al₂O₃ incorporation in MgSiO₃ perovskite and ilmenite. *Earth and Planetary Science Letters*, 252(1–2), 152–161. <https://doi.org/10.1016/j.epsl.2006.09.036>
- Petríček, V., Dušek, M., & Palatinus, L. (2014). Crystallographic computing system JANA2006: General features. *Zeitschrift Fur Kristallographie*, 229(5), 345–352. De Gruyter Oldenbourg. <https://doi.org/10.1515/zkri-2014-1737>
- Prescher, C., & Prakapenka, V. B. (2015). DIOPTAS: A program for reduction of two-dimensional X-ray diffraction data and data exploration. *High Pressure Research*, 35(3), 223–230. <https://doi.org/10.1080/08957959.2015.1059835>
- Ralph, R. L., & Finger, L. W. (1982). A computer-program for refinement of crystal orientation matrix and lattice-constants from diffractometer data with lattice symmetry constraints. *Journal of Applied Crystallography*, 15(Oct), 537–539. <https://doi.org/10.1107/S0021889882012539>
- Rudolph, M. L., Lekić, V., & Lithgow-Bertelloni, C. (2015). Viscosity jump in Earth's mid-mantle. *Science*, 350(6266), 1349–1352. <https://doi.org/10.1126/science.1251929>
- Shannon, R. D. (1976). Revised effective ionic radii and systematic studies of interatomic distances in halides and chalcogenides. *Acta Crystallographica Section A*, 32(5), 751–767. <https://doi.org/10.1107/S0567739476001551>
- Sheldrick, G. M. (2015a). Crystal structure refinement with SHELXL. *Acta Crystallographica, Section C: Structural Chemistry*, 71(1), 3–8. <https://doi.org/10.1107/S2053229614024218>
- Sheldrick, G. M. (2015b). Foundations and Advances SHELXT-Integrated space-group and crystal-structure determination. *Acta Crystallographica*, 71(1), 3–8. <https://doi.org/10.1107/S2053273314026370>
- Sinogeikin, S. V., Zhang, J., & Bass, J. D. (2004). Elasticity of single crystal and polycrystalline MgSiO₃ perovskite by Brillouin spectroscopy. *Geophysical Research Letters*, 31(6). <https://doi.org/10.1029/2004gl019559>
- Stixrude, L., & Lithgow-Bertelloni, C. (2005). Thermodynamics of mantle minerals – I. Physical properties. *Geophysical Journal International*, 162(2), 610–632. <https://doi.org/10.1111/j.1365-246X.2005.02642.x>
- Stixrude, L., & Lithgow-Bertelloni, C. (2011). Thermodynamics of mantle minerals – II. Phase equilibria. *Geophysical Journal International*, 184(3), 1180–1213. <https://doi.org/10.1111/j.1365-246X.2010.04890.x>
- Vanpeteghem, C. B., Angel, R. J., Ross, N. L., Jacobsen, S. D., Dobson, D. P., Litasov, K. D., & Ohtani, E. (2006). Al, Fe substitution in the MgSiO₃ perovskite structure: A single-crystal X-ray diffraction study. *Physics of the Earth and Planetary Interiors*, 155(1–2), 96–103. <https://doi.org/10.1016/j.pepi.2005.10.003>
- Walter, M. J., Kubo, A., Yoshino, T., Brodholt, J. P., Koga, K. T., & Ohishi, Y. (2004). Phase relations and equation-of-state of aluminous Mg-silicate perovskite and implications for Earth's lower mantle. *Earth and Planetary Science Letters*, 222(2), 501–516. <https://doi.org/10.1016/j.epsl.2004.03.014>
- Walter, M. J., Trønnes, R. G., Armstrong, L. S., Lord, O. T., Caldwell, W. A., & Clark, S. M. (2006). Subsolidus phase relations and perovskite compressibility in the system MgO-Al₂O₃-SiO₂ with implications for Earth's lower mantle. *Earth and Planetary Science Letters*, 248(1–2), 77–89. <https://doi.org/10.1016/j.epsl.2006.05.017>
- Wang, L., Liu, Z., Koizumi, S., Ballaran, T. B., & Katsura, T. (2023). Aluminum components in bridgmanite coexisting with corundum and the CF-phase with temperature. *Journal of Geophysical Research: Solid Earth*, 128(1), e2022JB025739. <https://doi.org/10.1029/2022JB025739>
- Yagi, T., Okabe, K., Nishiyama, N., Kubo, A., & Kikegawa, T. (2004). Complicated effects of aluminum on the compressibility of silicate perovskite. *Physics of the Earth and Planetary Interiors*, 143(1–2), 81–91. <https://doi.org/10.1016/j.pepi.2003.07.020>
- Yamamoto, T., Yuen, D. A., & Ebisuzaki, T. (2003). Substitution mechanism of Al ions in MgSiO₃ perovskite under high pressure conditions from first-principles calculations. *Earth and Planetary Science Letters*, 206(3–4), 617–625. [https://doi.org/10.1016/S0012-821X\(02\)01099-3](https://doi.org/10.1016/S0012-821X(02)01099-3)
- Zhang, J., & Weidner, D. J. (1999). Thermal equation of state of aluminum-enriched silicate perovskite. *Science*, 284(5415), 782–784. <https://doi.org/10.1126/science.284.5415.782>

References From the Supporting Information

- Akaogi, M., Kojitani, H., Morita, T., Kawaji, H., & Atake, T. (2008). Low-temperature heat capacities, entropies and high-pressure phase relations of MgSiO₃, ilmenite and perovskite. *Physics and Chemistry of Minerals*, 35(5), 287–297. <https://doi.org/10.1007/s00269-008-0222-x>
- Datchi, F., Dewaele, A., Loubeyre, P., Letoutlec, R., Le Godec, Y., & Canny, B. (2007). Optical pressure sensors for high-pressure–high-temperature studies in a diamond anvil cell. *High Pressure Research*, 27(4), 447–463. <https://doi.org/10.1080/08957950701659593>
- Funamori, N., Yagi, T., Utsumi, W., Kondo, T., Uchida, T., & Funamori, M. (1996). Thermoelastic properties of MgSiO₃ perovskite determined by in situ X ray observations up to 30 GPa and 2000 K. *Journal of Geophysical Research*, 101(B4), 8257–8269. <https://doi.org/10.1029/95jb03732>

- Katsura, T., Yokoshi, S., Kawabe, K., Shatskiy, A., Manthilake, M. A. G. M., Zhai, S., et al. (2009). *P-V-T* relations of MgSiO_3 perovskite determined by in situ X-ray diffraction using a large-volume high-pressure apparatus. *Geophysical Research Letters*, *36*(1), 2–7. <https://doi.org/10.1029/2008GL035658>
- Kono, Y., Irifune, T., Higo, Y., Inoue, T., Barnhoorn, A., Suetsugu, D., et al. (2010). *P-V-T* relation of MgO derived by simultaneous elastic wave velocity and in situ X-ray measurements: A new pressure scale for the mantle transition region. *Physics of the Earth and Planetary Interiors*, *183*(1–2), 196–211. <https://doi.org/10.1016/j.pepi.2010.03.010>
- Litasov, K. D., Gavryushkin, P. N., Dorogokupets, P. I., Sharygin, I. S., Shatskiy, A., Fei, Y., et al. (2013). Thermal equation of state to 33.5 GPa and 1673 K and thermodynamic properties of tungsten. *Journal of Applied Physics*, *113*(13). <https://doi.org/10.1063/1.4799018>
- Nishihara, Y., Doi, S., Kakizawa, S., Higo, Y., & Tange, Y. (2020). Effect of pressure on temperature measurements using WRe thermocouple and its geophysical impact. *Physics of the Earth and Planetary Interiors*, *298*, 106348. <https://doi.org/10.1016/j.pepi.2019.106348>
- Poirier, J.-P. (2000). *Introduction to the physics of the Earth's interior*. Cambridge University Press. <https://doi.org/10.1017/CBO9781139164467>
- Tange, Y., Nishihara, Y., & Tsuchiya, T. (2009). Unified analyses for *P-V-T* equation of state of MgO: A solution for pressure-scale problems in high *P-T* experiments. *Journal of Geophysical Research*, *114*(B3), B03208. <https://doi.org/10.1029/2008JB005813>
- Tange, Y., Kuwayama, Y., Irifune, T., Funakoshi, K. I., & Ohishi, Y. (2012). *P-V-T* equation of state of MgSiO_3 perovskite based on the MgO pressure scale: A comprehensive reference for mineralogy of the lower mantle. *Journal of Geophysical Research*, *117*(6), 1–12. <https://doi.org/10.1029/2011JB008988>